energies

MDPI

Article

Effects of Hydrogeological Heterogeneity on CO_2 Migration and Mineral Trapping: 3D Reactive Transport Modeling of Geological CO_2 Storage in the Mt. Simon Sandstone, Indiana, USA

Babak Shabani [1,*], Peng Lu [2], Ryan Kammer [1] and Chen Zhu [3]

[1] Indiana Geological and Water Survey, Indiana University, Bloomington, IN 47405, USA; rkammer@iu.edu
[2] Saudi Aramco, Dhahran 31311, Saudi Arabia; peng.lu@aramco.com
[3] Department of Earth and Atmospheric Sciences, Indiana University, Bloomington, IN 47405, USA; chenzhu@indiana.edu
* Correspondence: bshabani@iu.edu

Abstract: We used three-dimensional (3D), high-resolution simulations facilitated by parallel computation to assess the effect of hydrogeological heterogeneity in the Mt. Simon Sandstone on CO_2 plume evolution and storage and geochemical reactions in a portion of the Illinois Basin, Indiana. Two scenarios were selected to investigate the effects of the hydrogeological heterogeneity in 3D reactive transport simulations: a heterogeneous case with variable porosity and permeability, and a homogenous case with constant porosity and permeability. The initial pressure, temperature, and mineralogical distributions are consistently applied in both the heterogeneous case and the homogeneous case. Results indicate that including hydrogeological heterogeneity in 3D reservoir simulations for geological CO_2 storage significantly impacts modeling results for plume migration patterns, CO_2-water-mineral interaction, reservoir quality, and CO_2 plume containment. In particular, results indicate that (1) the CO_2 plume reached the top of the Mt. Simon Sandstone in the homogeneous case, but was restrained to the lower third of the formation when hydrogeologic heterogeneity was considered; (2) the dominant trapping mechanism in the heterogeneous case was mineral trapping (43%), while it was solubility trapping (47%) in the homogeneous case (at 10,000 years); (3) incorporating reservoir heterogeneity in the model leads to a higher likelihood of long-term containment.

Keywords: geological CO_2 storage; geochemical reactions; hydrogeological heterogeneity; reactive transport simulation

check for updates

Citation: Shabani, B.; Lu, P.; Kammer, R.; Zhu, C. Effects of Hydrogeological Heterogeneity on CO_2 Migration and Mineral Trapping: 3D Reactive Transport Modeling of Geological CO_2 Storage in the Mt. Simon Sandstone, Indiana, USA. *Energies* **2022**, *15*, 2171. https://doi.org/10.3390/en15062171

Academic Editor: Huazhou Li

Received: 11 February 2022
Accepted: 9 March 2022
Published: 16 March 2022

Publisher's Note: MDPI stays neutral with regard to jurisdictional claims in published maps and institutional affiliations.

Copyright: © 2022 by the authors. Licensee MDPI, Basel, Switzerland. This article is an open access article distributed under the terms and conditions of the Creative Commons Attribution (CC BY) license (https://creativecommons.org/licenses/by/4.0/).

1. Introduction

Geological CO_2 storage (GCS) is one of the most promising methods to mitigate the emission of CO_2 into the atmosphere at scales great enough for climate alteration purposes [1–3]. Among geological storage sites, deep saline aquifers provide the most significant capacity for CO_2 storage [4]. The inherent heterogeneity of these reservoirs complicates the simulation of the CO_2 storage process. Numerical multiphase flow and reactive transport modeling, which integrates chemical reactions with the transport of fluids in porous media, is a valuable tool for predicting the fate of CO_2 in the heterogenous underground formations over spatial and temporal scales beyond those achieved experimentally, bridging the gap between short-term experimental data and field observations [5–14]. In recent years, many researchers have studied the effect of reservoir heterogeneity on different aspects of GCS, including CO_2 injectivity [15,16], CO_2 storage [15,17], CO_2 trapping and caprock containment [18,19], CO_2 plume evolution [20–23], and CO_2 leakage [16,24].

Injected CO_2 is permanently stored underground via four trapping mechanisms: structural, solubility, residual, and mineral trapping [3]. In structural trapping, an overlying formation with very low permeability stops the continued upward movement of CO_2 in the

reservoir due to buoyancy; in solubility trapping, CO_2 dissolves into the formation brine and hydrocarbons; in residual trapping, separated CO_2 droplets remain in the pore space by capillary forces as the remaining CO_2 fluid passes through the reservoir; in mineral trapping, CO_2 reacts with formation minerals and organic matter, leading to immobile carbonate mineralization [25–27].

Understanding the effect of heterogeneity on mineral trapping is vital because it plays an essential role in GCS's long-term viability. However, incorporating mineral trapping of CO_2 in 3D field-scale GCS modeling has gained less attention due to three main reasons: first, mineral trapping was not a dominant trapping mechanism through the first several hundred years after CO_2 injection began [10,14]; second, including geochemical reactions in a dynamic simulation (i.e., reactive transport modeling) is computationally expensive and time-consuming [28,29]; third, mineralogical and formation water information is needed for accurate reactive transport models, and is often lacking.

Previous works studying mineralogical reactions in heterogeneous reservoirs include Hermanson [28], who studied the effect of stratigraphic heterogeneity on mineral dissolution and precipitation reactions using a hypothetical 2D model. The author used realistic hydrological and geochemical input data from the literature to build a reactive transport model. The author concluded that CO_2 mineral trapping depends on the distribution and type of heterogeneities, the initial formation water chemistry, and mineral composition. Furthermore, the author reported that the most significant geochemical reactions occurred within low-permeability layers. Tian and Pan [18] developed a 2D model with homogenous mineral composition to study the effect of porosity and permeability heterogeneity on caprock mineral alteration and containment in the Xingouzui Formation in the Jianghan Basin, China. They concluded that the case with hydrological heterogeneity resulted in a significantly different mineral alteration of the caprock than in the homogenous case. They also observed that heterogeneity led to slower vertical CO_2 migration and increased horizontal propagation in the reservoir. However, to date, 3D reactive transport models that investigate the effect of hydrological heterogeneity on CO_2 trapping and geochemical reactions are scarce.

This study aims (1) to assess the effect of hydrogeological heterogeneity on CO_2 plume evolution and storage and (2) to investigate the importance of porosity and permeability heterogeneity on geochemical reactions. To achieve this goal, we investigated a potential CO_2 storage reservoir in the Cambrian Mt. Simon Sandstone of the Illinois Basin, Indiana. Previous and ongoing studies of the Mt. Simon Sandstone in the Illinois Basin have confirmed that it is favorable for CO_2 storage. This formation consists mainly of sandstone and is overlain by a near-impermeable shale of the Cambrian Eau Claire Formation, an important aspect in evaluating GCS suitability. For this study, the Eau Claire Formation was considered impermeable, and interactions between the Mt. Simon Sandstone and Eau Claire Formation in regard to CO_2 injection were not explored.

We selected two scenarios to investigate the effects of heterogeneity in porosity and permeability in 3D reactive transport modeling: (1) a base case, where heterogeneity is applied to porosity and permeability, and (2) a homogeneous case, where both porosity and permeability are homogeneous throughout the reservoir. The initial pressure, temperature, and mineralogical distributions are consistently applied in both cases. Results of the two cases were compared to evaluate the importance of including heterogeneity in reactive transport studies of GCS.

Geological Settings

The Cambrian Mt. Simon Sandstone is largely comprised of massive, poorly sorted sandstones and unconformably overlies Precambrian basement rocks throughout much of the Illinois Basin [30]. It is typically separated into upper, middle, and lower units, with an arkosic interval often present at the base of the Lower Mt. Simon [30–32]. Porosity and permeability of the Mt. Simon tend to increase with depth, likely caused by dissolution and large grain size within the arkosic unit of the Lower Mt. Simon [32,33]. The Mt. Simon

is thickest near the depocenter of the Illinois Basin, reaching more than 790-m-thick, and thins outward, especially toward the south, where it is not present in parts of southern Illinois [32]. The total storage resource estimate (SRE) for the Mt. Simon in the Illinois Basin ranges from 11.7 $GtCO_2$ to 161.1 $GtCO_2$ [34]. The primary seal for GCS in the Mt. Simon is the overlying Cambrian Eau Claire Formation, which is predominantly shale and ranges from 30- to 300-m-thick [31,35].

Additional deep saline formations that have been considered for GCS in the Illinois Basin include the Cambrian Potosi Dolomite and the Ordovician St. Peter Sandstone [36–38]. The Potosi Dolomite is a member of the Cambro-Ordovician Knox Supergroup and is known for vuggy and cavernous porosity [39]. While basin-scale SREs for the Potosi are not available, the SRE for the Knox Supergroup for the Illinois Basin ranges from 27.7 $GtCO_2$ to 239.7 $GtCO_2$ [34]. The St. Peter Sandstone ranges in thickness from 10 to 200 m, with the central and southern portions of the Illinois Basin meeting the criteria necessary for GCS [38,40,41]. The SRE for the St. Peter Sandstone in the Illinois Basin ranges from 579.9 $MtCO_2$ to 6.1 $GtCO_2$ [34].

The Maquoketa Group shale is considered a potential regional seal for sequestration for both the St. Peter Sandstone and the Potosi Dolomite, though other members in the Knox Supergroup, as well as the Ordovician Ancell Group and Black River Formation overlying the Knox, are also considered seals for the Potosi Dolomite [42,43]. Impermeable members of the Knox and the Maquoketa shale can also be considered secondary and tertiary sealing units, respectively, for the Mt. Simon.

Large-scale GCS projects in the Illinois Basin have focused on the Mt. Simon Sandstone as the primary reservoir to date (Figure 1a). The Illinois Basin—Decatur Project (IBDP) injected a total of one million tonnes of CO_2 into the Lower Mt. Simon Sandstone from 2011 to 2014 [44]. This project was monumental in demonstrating the potential of large-scale CO_2 injection in deep saline formations and provided valuable data for characterizing the Mt. Simon Sandstone. One of the findings from this project was the distinction of the Cambrian Argenta Formation, previously considered part of the Lower Mt. Simon Sandstone [45,46]. The success of IBDP led to development of commercial operations at the Archer Daniels Midland facility in Decatur, IL, the IL-CCS project, which is conducting ongoing injection of CO_2 into the Mt Simon Sandstone. These projects have spurred further interest in GCS throughout the Illinois Basin, including in western Indiana, where depositional and diagenetic features in the Mt. Simon Sandstone may be different than observed in the central part of the Illinois Basin [47,48].

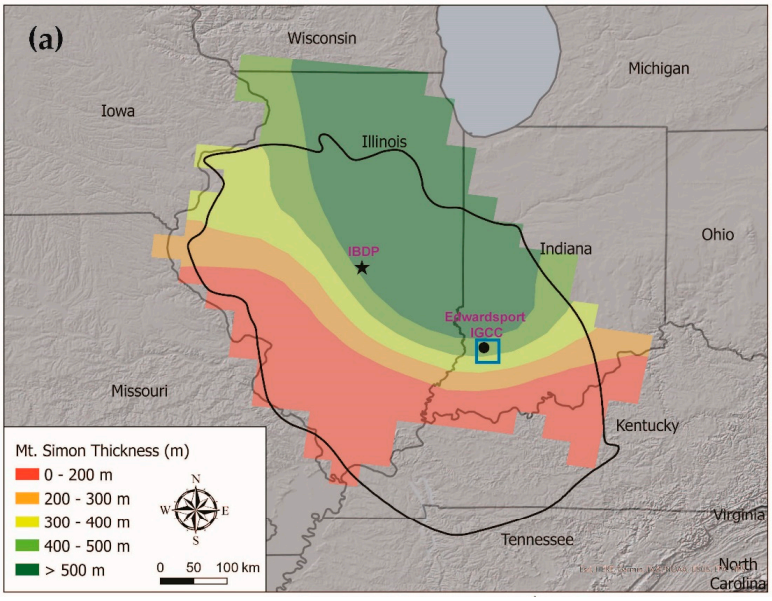


Figure 1. *Cont.*

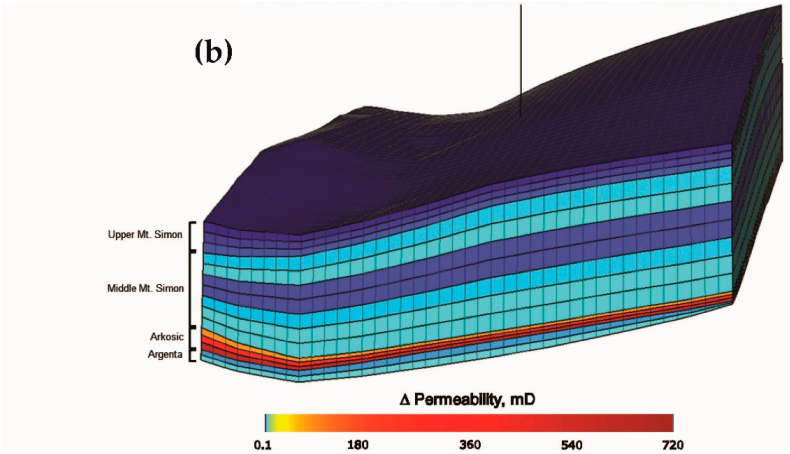


Figure 1. (**a**) Isopach map of the Mt. Simon throughout the Illinois Basin region in central U.S. showing the study area in blue rectangle, and (**b**) block diagram of the 3D permeability model of the study area.

In this study, we chose an area in southwest Indiana with GCS potential [49] to investigate the effect of hydrogeological heterogeneity in the Mt. Simon Sandstone on CO_2 plume evolution and storage and geochemical reactions. The area is associated with the Edwardsport integrated gasification combined cycle power plant (IGCC), which is a potential CO_2 source for GCS in the Illinois Basin [50].

2. Modeling Approach

2.1. Geological Model

The three-dimensional (3D) geologic model for this study was selected from the Indiana Mt. Simon Sandstone Petrel model provided by the Indiana Geological and Water Survey (Figures 1b and 2) [35,51,52]. The selected reservoir is in southwest Indiana in the vicinity of the Edwardsport deep well, which is one of the potential targets for geological CO_2 storage in the Illinois Basin. The model horizontally extends for 35 km and consists of four vertical units that, in descending order, are the Upper Mt. Simon Sandstone, Middle Mt. Simon Sandstone, Arkosic Mt. Simon Sandstone, and Argenta Formation (Figure 2). Vertical thickness changes throughout the model, with an average value of ~550 m. The minimum and maximum depths of the model are −1991 and −3214 m subsea (mss). All units are proportionally divided into 15 layers; ΔZ of each vertical layer varies with location, ranging between 2 and 67 m. The grid consists of 18,375 cells with a uniform ΔX and ΔY of 1000 m.

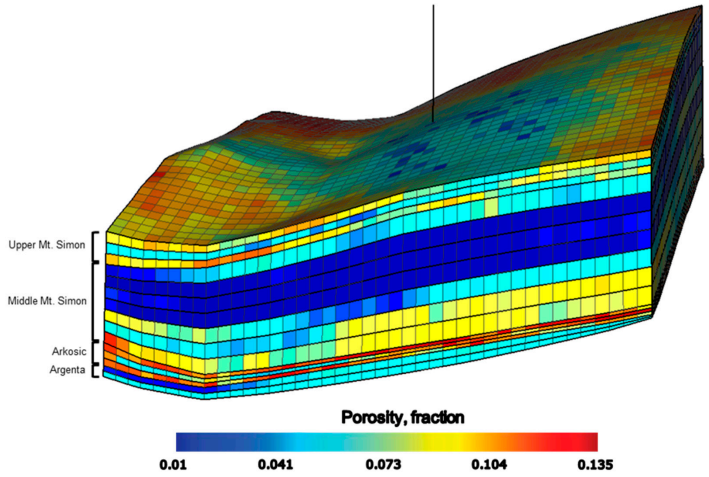


Figure 2. Block diagram illustrating the porosity of the reservoir. The model's size is approximately 35 km × 35 km × 550 m (x, y, z).

This study assumed the Mt. Simon Sandstone was overlain by the low-permeability Eau Claire Formation [35]; as such, the top boundary of the model was assumed to be closed to flow and transport. It was also assumed that the Mt. Simon Sandstone was underlain by Precambrian basement rock, consisting of low-permeability igneous rocks, so the lower boundary of the model was also considered to be closed to flow and transport. The left and right sides of the model were set to have constant reservoir pressure, temperature, and water chemistry.

2.2. Reactive Transport Simulator

Flow and reactive transport simulations of CO_2 and brine were conducted using the ECO2N module of TOUGHREACT V3.0-OMP V3.0 [53,54]. Open multi-processing (OMP) provides parallelization of chemical and coupling routines for significantly faster performance on multi-core shared memory computers. Hence, all simulations were carried out on the Big Red 3 supercomputer at Indiana University. Featuring 930 dual-socket compute nodes equipped with 22,464 compute cores, Big Red 3 theoretically has a peak performance of 934 trillion floating operations per second (https://kb.iu.edu/d/aoku (accessed on 7 March 2022)).

TOUGHREACT-ECO2N was used to simulate flow, transport, and chemical reactions of supercritical CO_2 with the Mt. Simon initially fully brine-saturated. The effect of salt on the phase partitioning of CO_2 and H_2O was considered. The precipitation and dissolution of minerals were dynamically coupled to porosity variations, and permeability was calculated as a function of porosity using the Kozeny–Carman equation. The simulations were conducted in isothermal mode, considering that heat transfer from chemical reactions was negligible.

2.3. Flow Properties and Initial Conditions of Pressure and Temperature

We conducted a 3D homogenous reservoir simulation as a baseline for comparison to assess the effect of porosity and permeability heterogeneity on CO_2 plume migration and mineral alteration.

In the heterogeneous case (base case), the porosity field was heterogeneously distributed throughout the model, ranging from 0.01 to 0.135 volume fraction (VF). Average vertical and horizontal permeability was used for each layer. Due to the lack of field and core data in the study area, the accurate estimation of the vertical-to-horizontal permeability ratio was not possible. Other studies on Mt. Simon reservoir characterization reported vertical-to-horizontal ratio from 0.016–1.0 [55]. Hence, we assumed the anisotropy ratio to be 0.1. The bottom of the Arkosic Mt. Simon has the highest horizontal permeability (up to 720 mD), and the top of the Upper Mt. Simon layer has the lowest horizontal permeability (as low as 0.1 mD).

The homogenous reservoir model is identical to the heterogeneous model except for porosity and permeability. The porosity and horizontal/vertical permeability of the homogenous model are 0.1 and 10 mD, respectively, throughout the reservoir.

The initial temperature field for both the base and homogenous cases was set using a linear regional geothermal gradient reflecting 62.3 °C and 92.0 °C at the top and bottom of the reservoir, respectively. The initial pressure was set at regional hydrostatic pressure, resulting in an initial steady-state condition with pressure ranging between 10.7 and 25.8 MPa throughout the reservoir.

The relative permeability and capillary pressure were each calculated as a function of water and gas saturation. Table 1 summarizes the model hydrogeological properties. Table 2 lists all symbols and notations.

Table 1. Hydrogeological properties of the model.

Parameter	Upper Mt. Simon	Middle Mt. Simon	Arkosic Mt. Simon	Argenta Formation
Porosity	0.02–0.13	0.01–0.12	0.03–0.135	0.01–0.07
Horizontal permeability (mD)	0.1–0.4	0.3–2.7	90–720	0.7–3.7
Capillary pressure (Van Genuchten) [a]	m = 0.457 S_{lr} = 0.3 P_0 = 65.8 kPa			
Relative permeability (Van Genuchten–Mualem) [b]	n = 0.58 S_{lr} = 0.3 S_{gr} = 0.1			

[a] $P_c = -P_0\left(S_*^{-1/m} - 1\right)^{1-m}$, $S_* = (S_l - S_{lr})/(1 - S_{lr})$. [b] $K_{rl} = \sqrt{S_*}\left\{1 - \left(1 - S_*^{1/n}\right)^n\right\}^2$, $K_{rg} = (1 - S_{**})^2 \times \left(1 - S_{**}^2\right)$, $S_{**} = (S_l - S_{lr})/\left(1 - S_{lr} - S_{gr}\right)$. P_c: Capillary pressure, P_0: Strength coefficient, m: Exponent, S_l: Water saturation, S_{lr}: Irreducible water saturation. K_{rl}: Relative permeability of water, K_{rg}: Relative permeability of gas, S_{gr}: Irreducible gas saturation, n: Exponent.

Table 2. List of symbols and definitions.

Symbol	Definition
A	Arrhenius pre-exponential factor (mol m^{-2} s^{-1})
a_i	Activity of species i
c_i	Molality of species i (mol kgw^{-1})
E_a	Apparent reaction activation energy (J mol^{-1})
$\Delta_r G$	Gibbs free energy of the dissolution reaction
J	Dissolution flux (mol·m^{-2} s^{-1})
K	Equilibrium constant
k	Rate constant (mol m^{-2} s^{-1})
k'	Rate coefficient (s^{-1})
m	Current moles of minerals per water mass (mol kgw^{-1})
m_0	Initial moles of minerals per water mass (mol kgw^{-1})
n_i	Reaction order for species i
p, q	Empirical exponents
Q	Reaction quotient
R	Universal gas constant (8.31446 J mol^{-1} K^{-1})
r	Reaction rate of mineral (mol kgw^{-1} s^{-1})
r_j	Reaction rate of mineral for mechanism j (mol kgw^{-1} s^{-1})
S_A	Surface area per unit water mass (m^{-2} kgw^{-1})
S_A^o	Initial surface area per unit water mass (m^{-2} kgw^{-1})
SI	Mineral saturation index (log Ω)
T	Temperature (K)
t	Time (s)
β_1, β_2	Correction parameters
v_i	Stoichiometry coefficient of reactant or product i in the reaction
ρ	Density of reactive surface sites on the mineral surface (mol m^{-2})
Ω	Mineral saturation quotient (Q/K)

2.4. Mineral and Formation Water Composition

The initial mineral composition is listed in Table 3. As the formation water contains a small amount of sulfur (Table 4), anhydrite is included as the potential secondary sulfate mineral. Gypsum is excluded because anhydrite is the stable thermodynamic phase within the range of formation temperatures in this study (~75 °C, on average).

The thermodynamic data of aqueous species and minerals are from Xu [56]. Calcite and anhydrite were set in equilibrium; all other minerals are kinetically controlled (Table 5). Prior to simulating reactive transport, a batch kinetic modeling of water-rock interaction is performed with the rate laws and kinetic data identical to the base case (Table 5). The chemical composition for the formation water (Table 4) is taken from Labotka [57]. In the batch model, the formation water reacted with the mineralogy of the Upper Mt. Simon Sandstone, Middle Mt. Simon Sandstone, Arkosic Mt. Simon Sandstone, and Argenta

Formation, for one million years. The resulting water compositions were used as the initial water in both models.

Table 3. Initial mineral volume fractions [a] and possible mineral phases used in the simulations.

Minerals Introduced in the Model	Chemical Formula	Upper Mt. Simon (%)	Middle-Arkosic Mt. Simon (%)	Argenta (%)
Quartz	SiO_2	68.4	83	82.5
K-feldspar	$KAlSi_3O_8$	22.2	12	11
Albite	$NaAlSi_3O_8$	2.1	1	1.5
Dolomite	$CaMg(CO_3)_2$	3.1	1.5	1
Illite	$K_{0.6}Mg_{0.25}Al_{1.8}(Al_{0.5}Si_{3.5}O_{10})(OH)_2$	3.1	1	3.5
Calcite	$CaCO_3$	1.1	1	0.5
Siderite	$FeCO_3$	0	0	0
Anhydrite	$CaSO_4$	0	0	0
Oligoclase	$Ca_{0.2}Na_{0.8}Al_{1.2}Si_{2.8}O_8$	0	0	0
Chlorite	$(Mg_{2.5}Fe_{2.5}Al)(AlSi_3)O_{10}(OH)_8$	0	0	0
Magnesite	$MgCO_3$	0	0	0
Kaolinite	$Al_2Si_2O_5(OH)_4$	0	0	0
Dawsonite	$NaAlCO_3(OH)_2$	0	0	0
Clinochlore	$Mg_5Al_2Si_3O_{10}(OH)_8$	0	0	0

[a] Modified from [57].

Table 4. Solution chemistry of the Mt. Simon Sandstone brine from [57].

Component	Concentration (mol/kg H_2O)
Ca^{2+}	4.95×10^{-1}
Mg^{2+}	9.1×10^{-2}
Na^{+}	1.988
K^{+}	5.2×10^{-2}
Fe	1.236×10^{-3} [a]
SO_4^{2-}	4.0×10^{-3}
Sr^{2+}	7.918×10^{-3}
Cl^{-}	3.202
Alkalinity	1.837×10^{-4} [a]
pH	6.35
Temperature	49 °C

[a] Ref. [58].

Table 5. Kinetic parameters in the model.

	Acid Mechanism				Neutral Mechanism			Base Mechanism			
	A mol m^{-2} s^{-1}	E_a kJ/mol	n_H	$\log k_{25}$	A mol m^{-2} s^{-1}	E_a kJ/mol	$\log k_{25}$	A mol m^{-2} s^{-1}	E_a kJ/mol	n_H	$\log k_{25}$
Anhydrite [1]	-	-	-	-	2.05×10^{-1}	14.3	−3.19	-	-	-	-
Dawsonite	-	-	-	-	1.01×10^{4}	62.8	−7.00	-	-	-	-
Magnesite	2.51×10^{6}	62.8	1.00	−4.60	45.7	62.8	−9.34	-	-	-	-
Oligoclase	51.3	65.0	0.46	−9.67	2.40	69.8	−11.84	5.01×10^{-5}	71.0	−0.57	−16.75
Calcite [2]	-	-	-	-	6.59×10^{4}	66.0	−6.74	-	-	-	-
Dolomite	3.21×10^{4}	46.0	0.61	−3.55	2.97×10^{-3}	31.0	−7.96	-	-	-	-
Kaolinite	2.56×10^{-4}	43.0	0.51	−11.12	5.00×10^{-8}	38.0	−13.96	2.87×10^{-3}	46.0	0.58	−10.60
K-feldspar	4.59×10^{-6}	31.0	0.27	−10.77	2.70×10^{-9}	31.0	−14.00	3.78×10^{-5}	31.0	0.35	−9.85
Quartz	-	-	-	-	1.98	77.0	−13.19	1.97×10^{4}	80.0	0.34	−9.72
Siderite	3.82×10^{4}	56.0	0.60	−5.23	13.6	56.0	−8.68	-	-	-	-
Chlorite [3]	1.00×10^{-4}	30.0	0.74	−9.26	4.70×10^{-11}	13.0	−12.61	1.50×10^{-9}	15.0	0.43	−11.45
Illite [4]	1.00×10^{-2}	58.0	0.55	−12.16	2.00×10^{-5}	54.0	−14.16	1.49×10^{-3}	77.0	0.35	−16.32
Albite	1.45	58.4	0.34	−10.07	4.97×10^{-10}	57.0	−19.29	7.41×10^{-1}	55.5	0.32	−9.85
Clinochlore	7.80×10^{-6}	17.0	0.28	−8.09	4.07×10^{-14}	16.0	−16.19	4.39×10^{-6}	16.0	0.34	−8.16

[1] Ref. [59]; [2] Ref. [60]; [3] Ref. [61]; [4] Ref. [8].

2.5. Model Initialization, Simulation Time, and CO_2 Injection Rate

The model was first set for a 10,000-year simulation time under natural conditions without performing reactive transport calculations to stabilize the reservoir pressure completely. The result of the pressure stabilization served as an initial flow condition for further simulations. Using the initial brine composition from the batch simulation and the initial flow condition from the pressure stabilization simulation, the reservoir was simulated for 100,000 years without any injection to reach a semi-steady-state condition.

Then, the resulting steady-state condition of pressure and quasi-state field of water and mineral compositions were used as initial conditions for the simulation of CO_2 injection. A vertical injection well was placed at the center of the model, penetrating all Mt. Simon units. This well was perforated in a 10-m interval at the bottom of the Arkosic Mt. Simon, which is the target reservoir for CO_2 storage in this study. CO_2 was injected at the rate of 30 kg/s (0.95 $MtCO_2$/year) for 30 years, followed by a 9970-year post-injection period. The maximum allowable time step was set at 3.65 days.

2.6. Kinetics of Mineral Reactions

Mineral dissolution or precipitation rate is the time-dependent concentration of reactants and products in the reaction system [62,63]:

$$r_{net} = \frac{1}{v_i}\frac{dC_i}{dt} \quad (1)$$

where r_{net} denotes net or overall mineral dissolution or destruction rate (mol kgw^{-1} s^{-1}), C_i is the concentration of a reactant or product (mol kgw^{-1}), t is the time (s), and v_i is the stoichiometry coefficient of reactant or product i in this reaction.

The mathematical equation of reaction rate can be defined as [64]:

$$r_{net} = S_A \sum_j A_j e^{-E_{a,\,j}/RT} \prod_i a_{i,\,j}^{ni} f(\Delta_r G) \quad (2)$$

$$k_j = A_j e^{-E_{a,\,j}/RT} \quad (3)$$

where j stands for a specific mechanism of the reaction, S_A is reactive surface area (m^2 kgw^{-1}), A_j is the Arrhenius pre-exponential factor (mol m^{-2} s^{-1}), $E_{a,j}$ is the apparent activation energy (J mol^{-1}), R is the universal gas constant (8.31446 J mol^{-1} K^{-1}), T is the temperature in Kelvin, and a_i is the activity of aqueous species i. $f(\Delta_r G)$ is the Gibbs free energy term of a dissolution reaction.

Palandri and Kharaka [59] defined the pH-dependence of reaction rates with H^+, H_2O, and OH^--promoted mechanisms:

$$k = k_{nu}^{25} exp\left[\frac{-E_{nu}}{R}\left(\frac{1}{T} - \frac{1}{298.15}\right)\right] + k_H^{25} exp\left[\frac{-E_H}{R}\left(\frac{1}{T} - \frac{1}{298.15}\right)\right] a_H^{n_H} + k_{OH}^{25} exp\left[\frac{-E_{OH}}{R}\left(\frac{1}{T} - \frac{1}{298.15}\right)\right] a_{OH}^{n_{OH}} \quad (4)$$

where subscripts *nu*, *H*, and *OH* indicate neutral, acid, and base mechanisms, respectively; k^{25} is the rate constant at 25 °C, E is the apparent activation energy, R is the universal gas constant, T is the absolute temperature, a is the activity of the aqueous species, and n is a power term.

In this study, the acid or base mechanism is considered for dissolution reactions, but not for precipitation reactions, which only uses a neutral pH mechanism. Table 5 lists the kinetic parameters [56]. The main geochemical reactions considered in the model are listed in Table 6.

Table 6. List of main geochemical reactions considered in the model.

Chemical Reaction
$CaCO_3$ (Calcite) + $H^+ \leftrightarrow HCO_3^-$ + Ca^{++}
$NaAlCO_3(OH)_2$ (Dawsonite) $\leftrightarrow H^+$ + HCO_3^- + Na^+ + AlO_2^-
$Al_2Si_2O_5(OH)_4$ (Kaolinite) $\leftrightarrow 2H^+ + 2SiO_2(aq) + H_2O + 2AlO_2^-$
$KAlSi_3O_8$ (K-feldspar) $\leftrightarrow K^+ + SiO_2(aq) + AlO_2^-$
SiO_2 (Quartz) $\leftrightarrow SiO_2(aq)$
$NaAlSi_3O_8$ (Albite) $\leftrightarrow Na^+ + 3SiO_2(aq) + AlO_2^-$
$K_{0.6}Mg_{0.25}Al_{2.3}Si_{3.5}O_{10}(OH)_2$ (Illite) $\leftrightarrow 1.2H^+ + 0.25Mg^{++} + 0.6K^+ + 3.5SiO_2(aq) + 0.4\ H_2O + 2.3AlO_2^-$

3. Results

3.1. CO_2 Plume Migration

3.1.1. Base Case

In general, the shape and size of the CO_2 plume are controlled by reservoir heterogeneity, viscous forces, capillary forces, and gravity forces (Figures 3 and 4). The simulated section of the reservoir deepens from northeast to southwest (Figure 1b). Hence, CO_2 tends to travel to the lower pressure directions of northeast and upward. CO_2 is injected in the high-permeability arkosic layer, which is confined by the low-permeability Argenta Formation and Middle Mt. Simon layer.

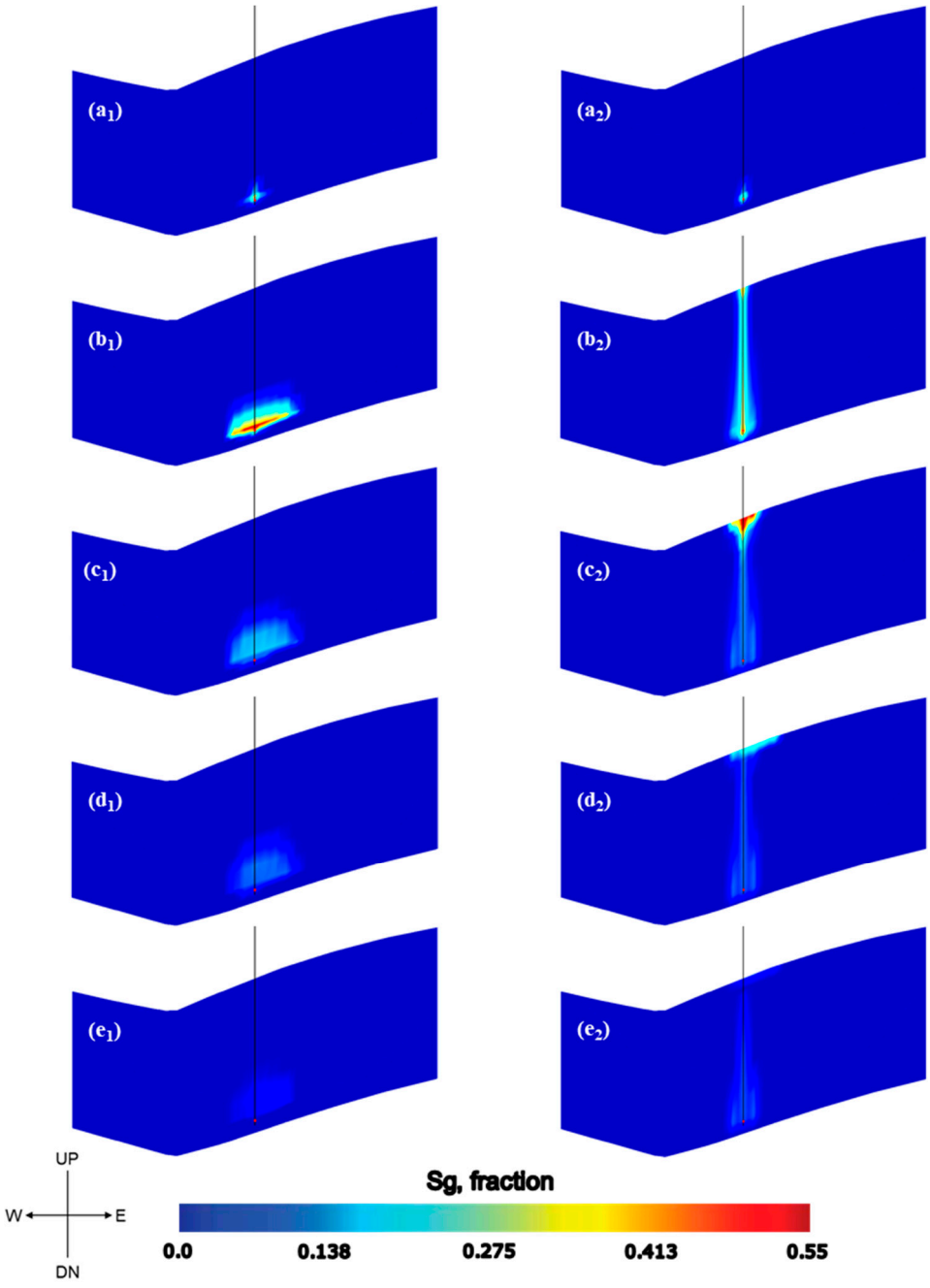


Figure 3. Fence diagrams illustrating the simulated Sg evolution for the base case ($\mathbf{a_1}$,$\mathbf{b_1}$,$\mathbf{c_1}$,$\mathbf{d_1}$,$\mathbf{e_1}$) and homogeneous case ($\mathbf{a_2}$,$\mathbf{b_2}$,$\mathbf{c_2}$,$\mathbf{d_2}$,$\mathbf{e_2}$) at (**a**) 1 year, (**b**) 30 years, (**c**) 100 years, (**d**) 1000 years, and (**e**) 10,000 years. Each figure's size is approximately 35 km × 550 m (x, z).

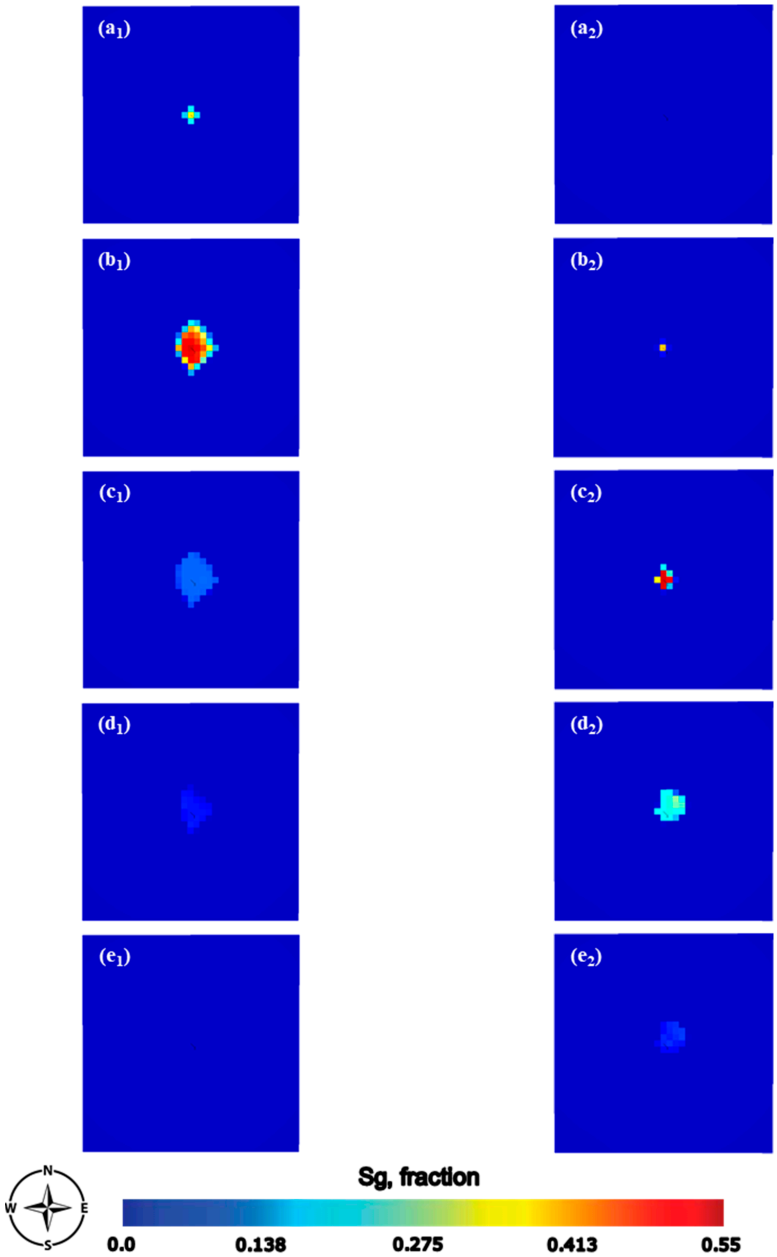


Figure 4. Plan view illustrations of simulated Sg evolution for the base case from the arkosic layer top view ($\mathbf{a_1}$,$\mathbf{b_1}$,$\mathbf{c_1}$,$\mathbf{d_1}$,$\mathbf{e_1}$) and homogenous case from the Upper Mt. Simon top view ($\mathbf{a_2}$,$\mathbf{b_2}$,$\mathbf{c_2}$,$\mathbf{d_2}$,$\mathbf{e_2}$) at (**a**) 1 year, (**b**) 30 years, (**c**) 100 years, (**d**) 1000 years, and (**e**) 10,000 years. Each figure's size is 35 km × 35 km (x, y).

During CO_2 injection, CO_2 propagates laterally in the high-permeability arkosic layer (Figure 3a_1–b_1). By the end of CO_2 injection, the maximum CO_2 plume distance from the injection point is about 5 km laterally (Figure 4b_1). During post-injection, CO_2 continues to move upward (Figure 3c_1–d_1). In the base case, CO_2 does not reach the caprock after 10,000 years of simulation (Figure 3e_1).

3.1.2. Homogenous Case

CO_2 plume migration in the homogeneous case differs significantly from the base case (Figures 3 and 4). In the homogeneous case, the gas migrates upward rapidly to develop into a conical cylinder after 30 years of injection (Figure 3b_2). After the CO_2 reaches the formation top, it spreads along the top of the formation and becomes pillar-

shaped at 100 years (Figure 3c_2). It continues to expand along the top of the formation until 1000 years (Figures 3d_2 and 4d_2). The CO_2 concentration at the top of the reservoir diminishes by 10,000 years (Figures 3e_2 and 4e_2). Most of the supercritical CO_2 that remains in the reservoir after 10,000 years of simulation is trapped in the lower layers (Figure 3e_2). The maximum CO_2 plume distance from the injection point is about 5 km laterally to the northeast (Figure 4d_2).

The most intense reactions and lateral movement in the base case occurs in the arkosic layer, and in the homogenous case they occur in the Upper Mt. Simon. Hence, these layers are considered good representatives of the simulations and are used in figures from the top view.

3.2. HCO_3^- and pH Variations

3.2.1. Base Case

The areal extent of the HCO_3^- profile is generally comparable with that of the CO_2 plume (Figures 3 and 5). The maximum total dissolved HCO_3^- concentration is 1.03 mol/kgw (Figure 5). Due to CO_2 dissolution, the area of high HCO_3^- increases, while Sg decreases in the same area (Figures 3 and 5).

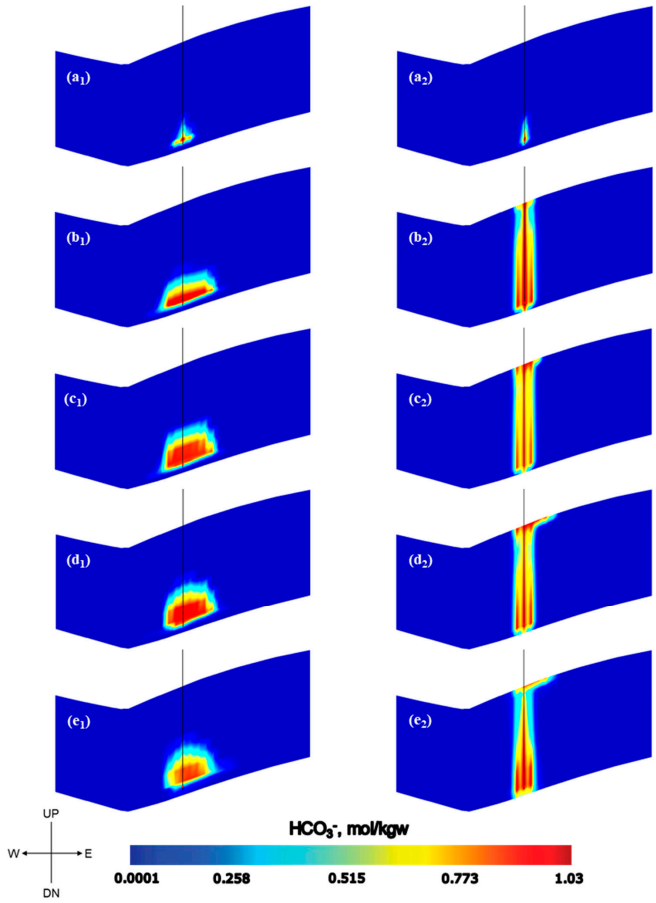


Figure 5. Fence diagrams of simulated HCO_3^- concentration (mol/kgw) evolution for the base case (**a_1**,**b_1**,**c_1**,**d_1**,**e_1**) and homogeneous case (**a_2**,**b_2**,**c_2**,**d_2**,**e_2**) at (**a**) 1 year, (**b**) 30 years, (**c**) 100 years, (**d**) 1000 years, and (**e**) 10,000 years. Each figure's size is approximately 35 km × 550 m (x, z).

The solution pH in the reservoir is controlled mainly by CO_2-water-rock interactions. The pH front migration is almost identical to the CO_2 plume migration and HCO_3^- front migration (Figures 5 and A1, and Figures 6 and A2). After one year of injection, the horizontal distribution of the pH front is nearly symmetrical (Figure A2a_1). The extent of the pH profile in the N-S direction is slightly larger than the E-W direction because

the reservoir dips from northeast to southwest (Figure A2b_1–c_1). Vertically, it forms a conical cylinder (Figure A1a_1). The pH value decreases from 8 (initial value) to ~4.8 near the injection well, due to the presence of carbonate acid generated by CO_2 dissolution. However, it buffers to ~6.8 near the pH front (Figures A1 and A2). After injection for 30 years, the pH front reaches ~6.5 km laterally and the shape of the plume becomes more asymmetric. The plume in the N-S direction is more elongated than that in the E-W direction because the reservoir dips toward the southwest, and buoyancy effects and plume development occur more in the east direction than in the west direction (Figure A2b_1). Similar to the CO_2 plume, the pH front develops more in the horizontal direction than in the vertical direction to become mushroom-shaped (Figure A1b_1). The reservoir pH in the middle of the plume increases to ~5. Since injection stops after 30 years, the size of the pH plume at 100 years is smaller than that at 30 years (Figure A2c_1) and slightly shrinks vertically (Figure A1c_1). The pH in the middle of the plume further increases to ~5.2 (Figure A1c_1). From 1000 to 10,000 years, the pH plume expands in the N-S direction and shrinks from the west of the injection well (Figure A1d_1–e_1). The pH in the middle of the plume further increases to ~5.6 at 1000 years and ~6.1 at 10,000 years (Figure A2d_1–e_1).

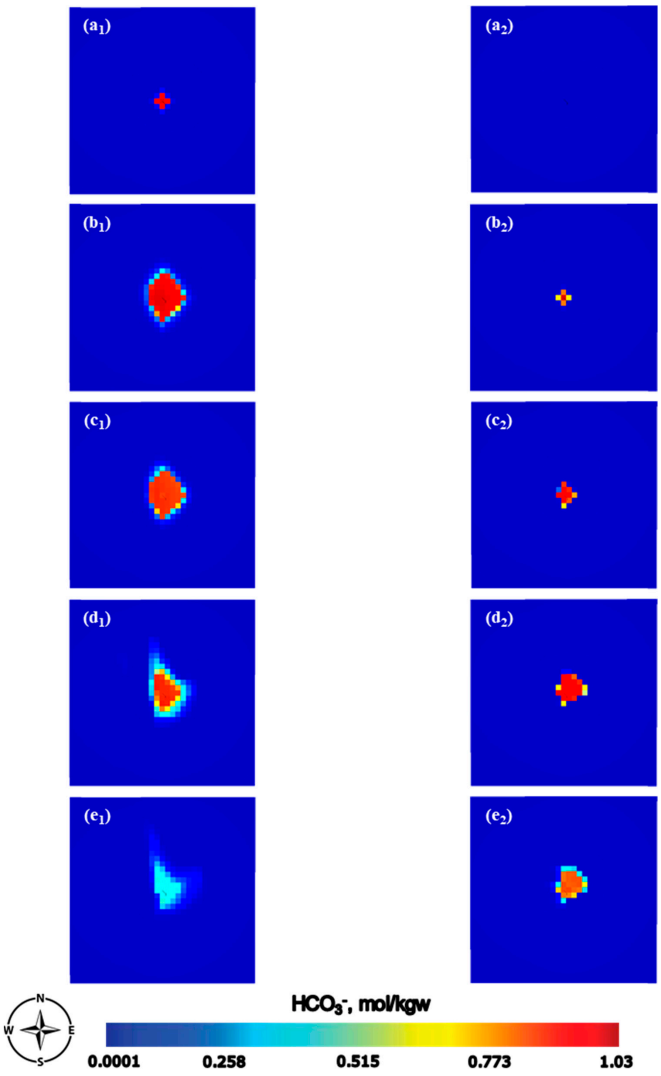


Figure 6. Plan-view diagrams illustrating the simulated HCO_3^- concentration (mol/kgw) evolution for the base case from the arkosic layer top view (**a_1**,**b_1**,**c_1**,**d_1**,**e_1**) and homogenous case from the Upper Mt. Simon top view (**a_2**,**b_2**,**c_2**,**d_2**,**e_2**) at (**a**) 1 year, (**b**) 30 years, (**c**) 100 years, (**d**) 1000 years, and (**e**) 10,000 years. Each figure's size is 35 km × 35 km (x, y).

3.2.2. Homogenous Case

Similar to the heterogeneous case, the areal extent of HCO_3^- is comparable with that of pH evolution and CO_2 plume (Figures 5 and A1, and Figures 6 and A2). The maximum total dissolved concentration of HCO_3^- is around 1.03 mol/kgw near the injection well after 1 yr of injection (Figure 5a_2), where the pH drops from 8 to ~4.8 (Figure A1a_2). However, pH buffers to ~6.8 at the front of the CO_2 plume. The HCO_3^- front moves upward until it reaches the caprock at 30 years (Figures 5b_2 and 6b_2), and expands under the caprock, primarily northeast, toward the lower pressure zone (Figures 5c_2–e_2 and 6c_2–e_2). The distributions of pH profiles are similar to those of CO_2 plume and HCO_3^- (Figures A1c_2–e_2 and A2c_2–e_2). The pH value in the middle of the plume further increases to ~5 at 1000 years and ~5.6 at 10,000 years (Figure A2d_1–e_1).

3.3. Mineralogical Evolutions

3.3.1. Coupled Reactions

Previous studies identified coupled K-feldspar dissolution with illite and quartz precipitation to be the dominant reaction in the Mt. Simon Sandstone system [10,14]. The overall reaction can be written as:

$$2.3\ KAlSi_3O_8\ (\text{K-feldspar}) + 0.25\ Mg^{2+} + 1.2\ H^+ + 0.4\ H_2O \rightarrow K_{0.6}Mg_{0.25}Al_{2.3}Si_{3.5}O_{10}(OH)_2\ (\text{illite}) + 3.4\ SiO_2\ (\text{quartz}) + 1.7\ K^+ \quad (5)$$

However, the mineralogy of the Mt. Simon varies throughout the Illinois Basin. In [10,14], the formation consists of 21.2% K-feldspar and 0.44% of oligoclase, but, in this study, the Mt. Simon consists of 11–22.2% K-feldspar and 1–2.1% albite, and oligoclase is absent. The presence of albite, high CO_2(aq) activity, and NaCl-dominated formation water prefers the formation of dawsonite [13]:

$$CO_2(aq) + H_2O + NaAlSi_3O_8\ (\text{albite}) \rightarrow 3SiO_2\ (\text{quartz}) + NaAlCO_3(OH)_2\ (\text{dawsonite}) \quad (6)$$

Therefore, the coupled reaction of dawsonite and quartz precipitation at the expense of albite is also important in the studied system.

3.3.2. Feldspar Dissolution

Base case K-feldspar dissolution: The dissolved K-feldspar exhibited three differentiated dissolution zones at 1000 years, including (1) the moderate dissolution zone (e.g., dissolved ~0.0023 VF of K-feldspar at 1000 years) in the high HCO_3^- concentration zone in the middle of the plume, (2) the intensive dissolution zone (e.g., dissolved ~0.0035 VF of K-feldspar at 1000 years) at the gas-water contact, and (3) the gentle dissolution zone (e.g., dissolved ~0.001 VF of K-feldspar at 1000 years) outside of the gas-water contact and extending into the water zone) (Figure 7c_1). The formation of the intensive dissolution zone is likely due to more illite precipitation (Figure A6). Illite precipitation consumes K^+, which promotes K-feldspar dissolution (Equation (5)). Dawsonite precipitation mainly occurs in the moderate dissolution zone (Figure A3c_1), where less illite precipitates (Figure A6). At 10,000 years, an extensive dissolution zone (up to ~0.0103 VF of dissolved K-feldspar) at the gas-water contact to the west of the CO_2 plume, and a K-feldspar precipitation zone (up to ~0.00025 VF of precipitated K-feldspar) at the gas-water contact to the east of the plume occurs (Figure 7d_1). The gentle dissolution zone extends to the southeast, but the amount of dissolved K-feldspar remains almost the same (dissolved ~0.001 VF of K-feldspar) (Figure 7d_1).

Homogenous case K-feldspar dissolution: Compared to the base case, the areal coverage of the K-feldspar dissolution zone is much smaller, but the dissolution is more intensive. Like the base case, dissolved K-feldspar exhibited three differential dissolution zones at 1000 years (Figure 7c_2) in the homogenous case. This is also related to the differentiated illite and dawsonite precipitation (Figures A3 and A6). At 10,000 years, K-feldspar dissolution reached up to ~0.006 VF.

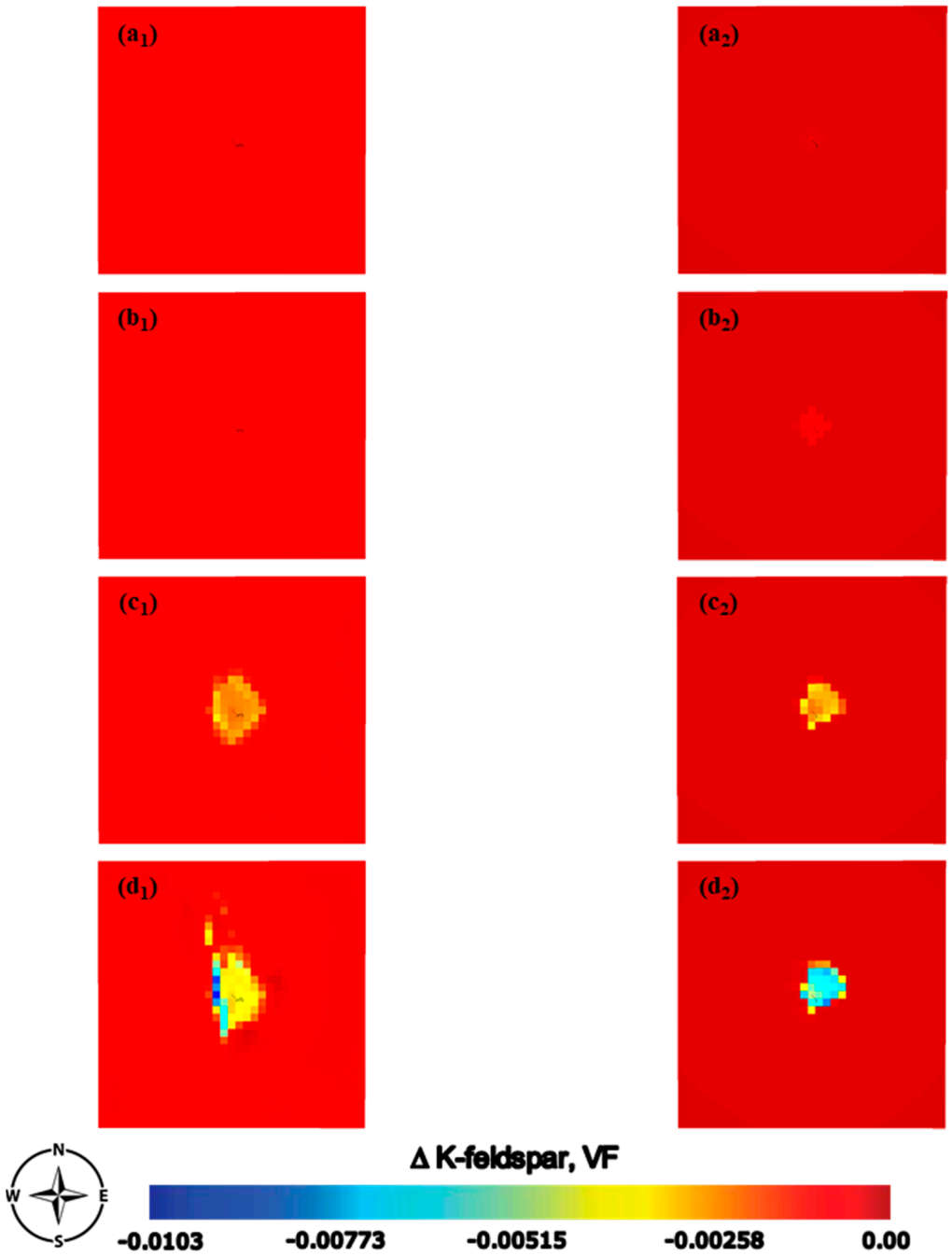


Figure 7. Plan view diagrams illustrating the simulated Δ K-feldspar volume fraction evolution for the base case from the arkosic layer top view (**a**$_1$,**b**$_1$,**c**$_1$,**d**$_1$) and homogenous case from the Upper Mt. Simon top view (**a**$_2$,**b**$_2$,**c**$_2$,**d**$_2$) at (**a**) 30 years, (**b**) 100 years, (**c**) 1000 years, and (**d**) 10,000 years. Each figure's size is 35 km × 35 km (x, y).

Base case albite dissolution: The dissolution of albite was promoted by the high HCO_3^- concentrations to form quartz and dawsonite (Equation (6)). The distribution of dissolved albite is roughly comparable with the distribution of HCO_3^- (Figures 6 and 8). The amount of dissolved albite increases to ~0.001 VF at 100 years and ~0.0025 VF at 1000 years (Figure 8b$_1$–c$_1$). At 10,000 years, ~0.006 VF albite is dissolved near the injection well and the dissolved amounts decrease outward, forming a halo-like profile (Figure 8d$_1$).

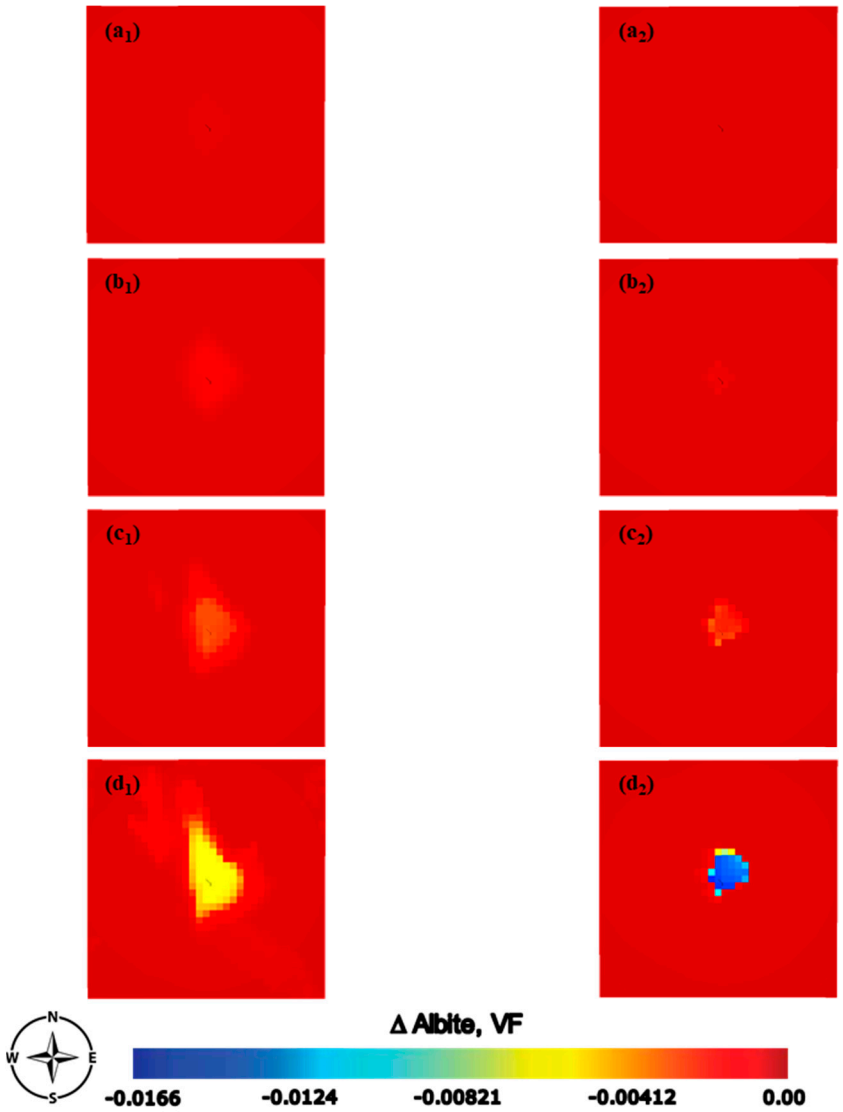


Figure 8. Plan view diagrams illustrating the simulated Δ albite volume fraction evolution for the base case from the arkosic layer top view ($\mathbf{a_1}$,$\mathbf{b_1}$,$\mathbf{c_1}$,$\mathbf{d_1}$) and homogenous case from the Upper Mt. Simon top view ($\mathbf{a_2}$,$\mathbf{b_2}$,$\mathbf{c_2}$,$\mathbf{d_2}$) at (**a**) 30 years, (**b**) 100 years, (**c**) 1000 years, and (**d**) 10,000 years. Each figure's size is 35 km × 35 km (x, y).

Homogeneous case albite dissolution: Similarly, the distribution of dissolved albite is roughly comparable with the distribution of HCO_3^- (Figures 6 and 8). Compared to the base case, the areal coverage of the albite dissolution zone is much smaller, but the dissolution is more intensive. At 10,000 years, albite is almost completely exhausted (~0.014 VF) near the injection well and the dissolved amounts decrease outward (Figure 8d_2).

3.3.3. Secondary Silicate Mineral Precipitation

Base case quartz precipitation: The distribution of precipitated quartz is roughly comparable with those of dissolved albite and high HCO_3^- (Figures 6, 8 and A5). The amount of quartz precipitation increases to ~0.001 VF at 100 years and ~0.0025 VF at 1000 years (Figure A5b_1–c_1). At 10,000 years, it reaches ~0.0045 VF near the injection well and decreases outward, forming a halo-like profile (Figure A5d_1).

Homogeneous case quartz precipitation: Compared to the base case, the areal coverage of the quartz precipitation zone is much smaller, but the precipitation is more intensive. At 10,000 years, it reaches ~0.013 VF near the injection well (Figure A5d_2).

Base case illite precipitation: The distribution of precipitated illite is roughly comparable with that of dissolved K-feldspar to form the moderate, intensive, and gentle precipitation zones (Figures 7 and A6). At 10,000 years, it reaches ~0.007 VF at the intensive precipitation zone (Figure A6d_1).

Homogeneous case illite precipitation: Compared to the base case, both the areal coverage of the precipitation zone and the intensity are much smaller. At 10,000 years, it reaches ~0.004 VF at the intensive precipitation zone (Figure A6d_2).

3.3.4. Secondary Carbonate Mineral Precipitation

We focused on calcite and dawsonite for secondary carbonate minerals only because ankerite, dolomite, magnesite, and siderite were insignificant.

Base case dawsonite precipitation: The distribution of dawsonite is limited to the high HCO_3^- concentration area (>0.25 mol/kgw; Figures 5 and A3). The extent of the dawsonite precipitation area and the amount precipitated continuously increase during 0–100 years (Figure A3a_1–b_1). At 1000 years, the extent of the precipitation area slightly decreases, but the amount of precipitation increases (Figure A3c_1). The maximum abundance of dawsonite increases to ~0.002 VF near the dawsonite front. At 10,000 years, the extent of the precipitation area further decreases, but the abundance of dawsonite increases, up to 0.0035 VF (Figure A3d_1). The dawsonite abundance decreases outward from the injection well. In the dawsonite dissolution zone, more K-feldspar dissolves (Figure 7d_1), and pH increases to ~7 (Figure A2e_1). Lower HCO_3^- concentration and higher pH make dawsonite unstable and convert it to calcite instead.

Homogeneous case dawsonite precipitation: Similarly, the distribution of dawsonite is limited to the high HCO_3^- concentration area (>0.25 mol/kgw; Figure 5). The extent of the dawsonite precipitation area and the amount precipitated continuously increases, and the area of the dawsonite precipitation zone is consistent with that of the albite dissolution zone (Figures 8 and A3). At 10,000 years, the amount of dawsonite precipitated reaches ~0.0096 VF (Figure A3d_2), about three times higher than that in the base case.

Base case calcite precipitation: The distribution of calcite cement is generally comparable with the distribution of the high pH zone (pH > 5.6) (Figures A1 and A4). It becomes increasingly asymmetric after 1000 years due to the reservoir heterogeneity (Figure A4). During 1000–10,000 years, the dissolved dawsonite mainly converts to calcite (Figures A3c_1–d_1 and A4c_1–d_1). At 10,000 years, it reaches ~0.0015 VF (Figure A4d_1) at the intensive K-feldspar dissolution zone.

Homogeneous case calcite precipitation: Compared to the base case, calcite precipitated, in this case, is relatively insignificant. At 10,000 years, it only reaches ~0.0004 (Figure A4d_2) at the intensive K-feldspar dissolution zone.

3.4. Porosity and Permeability Changes

Base case porosity changes: At 100 years, there is a slight decrease of porosity near the injection well and a slight increase outside the porosity reduction zone (Figure A7b_1). The decreased zone is roughly comparable with the high quartz and dawsonite precipitation zone (Figures A5b_1 and A3b_1) and is caused by more quartz and dawsonite precipitation than albite dissolution. At 1000 years, porosity further decreases at the porosity reduction zone and increases outside of it (Figure A7c_1). Generally, the porosity changes are insignificant during 0–1000 years (~0.00015 VF). However, at 10,000 years, there is an enhanced porosity generation zone outside of the porosity reduction zone (Figure A7d_1), which is likely due to more K-feldspar dissolution than secondary mineral precipitation. Up to 0.0014 VF porosity is generated in this zone. Outside of the porosity generation zone, there is another porosity reduction zone with slight porosity reduction. At 10,000 years, the distribution of Δ porosity zones are roughly comparable with the Δ K-feldspar dissolution zone (Figures 7d_1 and A7d_1).

We evaluated the mineralogical contributions to the porosity changes in a cell near the injection well (Figure A9). K-feldspar dissolution is the most important contributor to the

porosity generation, followed by albite dissolution, while dawsonite precipitation plays the most important role in porosity reduction followed by illite precipitation.

Homogeneous case porosity changes: Compared to the base case, the size of the porosity change zone in the homogeneous case is much smaller. A slight porosity generation occurs near the injection well from 30–100 years (Figure A7a_2–b_2), due to more K-feldspar and albite dissolution than secondary mineral precipitation. However, from 1000–10,000 years, a porosity reduction zone occurs near the injection well (Figure A7c_2–d_2), which correlates well with the dawsonite precipitation zone (Figure A3c_2–d_2). At 10,000 years, the porosity reduction reaches up to ~0.0045 VF.

Albite dissolution is the most important contributor to the porosity generation, followed by K-feldspar dissolution and dawsonite precipitation plays the most important role in porosity reduction followed by illite precipitation (Figure A10). The conversion of albite to dawsonite plays much important role in porosity changes in the homogeneous case than that in the base case.

Base case permeability changes: Permeability changes are generally correlated with porosity changes and become more evident after 1000 years. At 1000 years, permeability decreases up to 2 mD at the porosity reduction zone and increases up to 2 mD at the porosity generation zone (Figure A8a_1). At 10,000 years, permeability decreases up to 3 mD at the porosity reduction zone and increases up to 5 mD at the porosity generation zone (Figure A8b_1).

Homogeneous case permeability changes: Similarly, the permeability changes in the homogeneous case also correlate to porosity changes. At 10,000 years, the porosity reduction reaches up to ~1 mD near the injection well.

4. Discussion

4.1. Competitions of K-Feldspar and Albite Dissolution

The carbonate mineral precipitation is related to CO_2-driven feldspar dissolution. In the base case, coupled K-feldspar dissolution and illite precipitation (Equation (5)) is dominant and coupled albite dissolution and dawsonite precipitation (Equation (6)) is minor. Reactions in Equation (5) will raise the pH to 5.6 or higher and promote calcite precipitation. However, in the homogenous case, Equation (6) is dominant, and Equation (5) is minor. Dawsonite precipitation requires high pCO_2 or high HCO_3^- concentration; it usually occurs near the injection well.

Albite dissolution was focused at the high HCO_3^- concentration zone in both cases. This is because high HCO_3^- concentration (and activity) facilitated the precipitation of dawsonite when Na^+ concentration (and activity) was high and because dawsonite precipitation removed Na^+ from the solution, which, in turn, promoted albite dissolution (Equation (6)).

There was more dissolved K-feldspar than dissolved albite outside of the high HCO_3^- concentration zone. For example, the dissolved amount of K-feldspar was ~0.002 VF at 100 years, while it was ~0.001 VF for albite in the base case (Figures 7b_1 and 8b_1). This is likely due to (1) K-feldspar's higher initial surface area due to its high mineral abundance, and (2) high Na^+ concentration (~2 M) in the solution inhibiting the dissolution of albite.

Both albite and K-feldspar dissolution release $SiO_2{}^o$(aq). Because of slow quartz and illite precipitation (Table 5), $SiO_2{}^o$(aq) remained high in the high HCO_3^- concentration zone due to more albite dissolution in this zone, which suppressed the dissolution of K-feldspar (i.e., the common ion effect). Therefore, there was a competition between K-feldspar and albite dissolution; albite dissolution was preferred at the high HCO_3^- concentration zone and K-feldspar dissolution was preferred outside this zone.

4.2. Temporary Presence of Dawsonite

Dawsonite is proposed to be a major carbon sink for mineral trapping in geological carbon sequestration. However, dawsonite has only limited geological occurrences, and the plausibility of dawsonite formation in GCS carries lingering doubts. It is found that,

using a thermodynamic phase diagram and one-dimensional reactive transport modeling, high Na and C concentrations are required to form dawsonite [65]. Additionally, dawsonite is unstable in the general reservoir conditions for GCS and will redissolve if the CO_2 partial pressure drops. The area of dawsonite redissolution during 1000–10,000 years was found to be consistent with the area of the decreased HCO_3^- concentrations in the base case (Figures 6d_1–e_1 and A3c_1–d_1). At 10,000 years, there is still a significant amount of dawsonite (up to 0.0032 VF) present near the injection well, which corresponds to the zone with high HCO_3^- concentration. IPCC indicates that "a delay in emissions in the order of a thousand years may be almost as effective as perfect storage." [3] Though it may ultimately redissolve, mineral trapping by dawsonite is still a very important carbon sink mechanism.

In contrast, redissolution of dawsonite is not observed in the homogeneous case even at 10,000 years (Figure A3d_2). This is due to HCO_3^- concentration remaining quite high (~0.9 M) at 10,000 years (Figure 6e_2).

4.3. Effects of Reservoir Heterogeneity

The homogeneous case is compared with the results from the base case to illustrate the effects of reservoir hydrogeological heterogeneity on CO_2 plume migration, CO_2-water-rock interactions and trapping mechanisms, and CO_2 plume containment.

4.3.1. Differences in the CO_2 Plume Migration

In the base case, the distribution of CO_2 gas is restrained within the lower third of the formation (Middle Mt. Simon and below) and never reaches the top layer (Upper Mt. Simon layer), causing the CO_2 plume to be mushroom-shaped. This is because the Middle Mt. Simon layer has low permeability (vertical permeability: 0.03–0.27 mD) and prevents CO_2 from migrating upward.

During CO_2 injection, viscous and buoyancy forces dominate, leading to CO_2 propagating laterally in the high-permeability arkosic layer. This leads to CO_2 moving upward to the top of the arkosic layer due to buoyancy effects, and then expanding laterally (the highly concentrated CO_2 plume in red in Figure 3a_1–b_1). This is similar to the typical CO_2 movement in high-permeability isotropic homogenous reservoirs, where CO_2 moves mostly upward during CO_2 injection until it reaches an impermeable or low-permeability area and then expands laterally.

During post-injection, CO_2 continues to move upward due to buoyancy, until capillary forces balance buoyancy factors. In the base case, CO_2 does not reach the caprock after 10,000 years of simulation (Figure 3d_1).

In the homogenous case, the injected CO_2 primarily migrates vertically until it reaches the top of the reservoir and then expands up dip in the N-E direction. Due to a consistent higher vertical permeability in the homogenous case and a lower horizontal permeability, the buoyancy effect dominates lateral viscous forces, resulting in upward movement of the gas toward the upper low-pressure regions for 1000 years (Figures 3d_2 and 4d_2). Then, gas concentration gradually decreases because of the mineral and solubility trapping domination. The remaining gas in the reservoir after 10,000 years of simulation traps in the lower layers by capillary forces (Figure 3e_2). It can be predicted that the remaining gas will eventually vanish because of the mineral reactions and solubility mechanism. The lateral expansion of CO_2 in the base case is greater than the homogenous case. This is mainly due to the high horizontal permeability of the arkosic layer and the low permeability of the overlying layer in the base case.

4.3.2. Differences in the CO_2-Water-Rock Interactions

In both base and homogeneous cases, the areal extension of the HCO_3^- front is consistent with the CO_2 plume (Figures 3 and 5). The pH front had higher pH near the edge and lower pH at the center (Figures 6 and A2). The distribution of pH in the homogeneous case is more symmetric than in the base case because the CO_2 plume developed less in the

lateral directions in the homogeneous case. At 10,000 years, pH in the middle of the plume is ~6.1 in the base case but increases to ~6.5 in the homogenous case.

For K-feldspar, albite, and quartz, the areal distribution of dissolution and precipitation reactions are smaller and more symmetric in the homogenous case than those in the base case, but the reactions were more intense in the reaction zones. However, for illite, both the areal distribution and the intensity were smaller in the homogenous case than in the base case.

In the homogenous case, the coupled albite dissolution-dawsonite (and quartz) precipitation reaction was more important than the coupled K-feldspar dissolution-illite precipitation reaction in the study site, especially near the injection well, while in the base case coupled K-feldspar dissolution-illite precipitation reaction was more important.

In the base case, the total precipitated calcite (in terms of volume fractions) is comparable with that of dawsonite. However, in the homogenous case, dawsonite is the predominant carbonate cement precipitated and the amount of calcite precipitation is negligible.

4.3.3. Porosity and Permeability Differences

Unlike the base case, porosity generation in the homogeneous case is negligible (Figure A7). Porosity reduction of up to 0.0045 VF is observed near the injection well at 10,000 years (Figure A7d_2) that is caused by more dawsonite precipitation than albite and K-feldspar dissolution. Similar to porosity, permeability decreases mostly during 1000–10,000 years with a maximum of 1 mD reduction near the injection well at 10,000 years (Figure A8).

The comparison of change in volume fraction for different mineral dissolution and precipitation along with the porosity and permeability alteration is shown in Figures A9 and A10. The demonstrated results are taken from a cell near the injection well in the arkosic layer for the base case, and from the top of the reservoir in the homogenous case. This cell is representative of the area where the HCO_3^- availability is high. The results also prove that the combination of K-feldspar dissolution-illite precipitation is a dominant mineral reaction in the base case, while the albite dissolution-dawsonite precipitation is dominant in the homogenous case.

4.3.4. CO_2 Plume Containment

The behavior of CO_2 plume development has significant impacts on the safety and security of CO_2 storage. In the base case, the CO_2 plume developed more laterally than vertically. The lower permeability Middle Mt. Simon layer acted as the first caprock, and the low permeability Upper Mt. Simon layer worked as the second caprock. With the two layers of caprocks to prevent upward migration of CO_2, the risk of CO_2 leakage in this site can be regarded as very low. This leakage rate means that the Mt. Simon Sandstone itself has the capacity to retain all the injected CO_2 safely, and the Eau Claire Shale can provide extra security to prevent leakage.

However, in the homogeneous case, upward migration dominates CO_2 plume migration. Within 30 years, the plume quickly travels the entire thickness of the formation to reach the formation top and then spreads out along the top of the unit. In this case, the CO_2 leakage potential will depend on the sealing capacity of overlaying formations (i.e., the Eau Claire Shale).

The differences in the behavior of CO_2 plume development for the two cases also affect the trapping mechanisms. CO_2 plume migration in the subsurface is a complex process and generally involves four storage mechanisms: (1) structural and hydrodynamic trapping; (2) residual trapping; (3) solubility trapping; and (4) mineral trapping. Of these four processes, mineral trapping is considered the safest trapping mechanism for long-term CO_2 storage [66]. In this study, gas trapping is defined as a combination of structural and hydrodynamic trapping and residual trapping.

For the base case, solubility trapping begins at ~35% and increases to ~45% at 1 year, (Figure 9), and gradually decreases to ~30% at 30 years. During the post-injection period,

solubility trapping gradually increases to ~40% at 100 years. After ~3000 years, the percentage slightly decreases and reaches ~37% at 10,000 years. Mineral trapping does not occur until ~200 years, and its percentage steadily increases to ~43% by the end of the simulation. More than half of the injected CO_2 is in gas form until ~700 years, after which the gas trapping gradually decreases to ~20% at the end of the simulation.

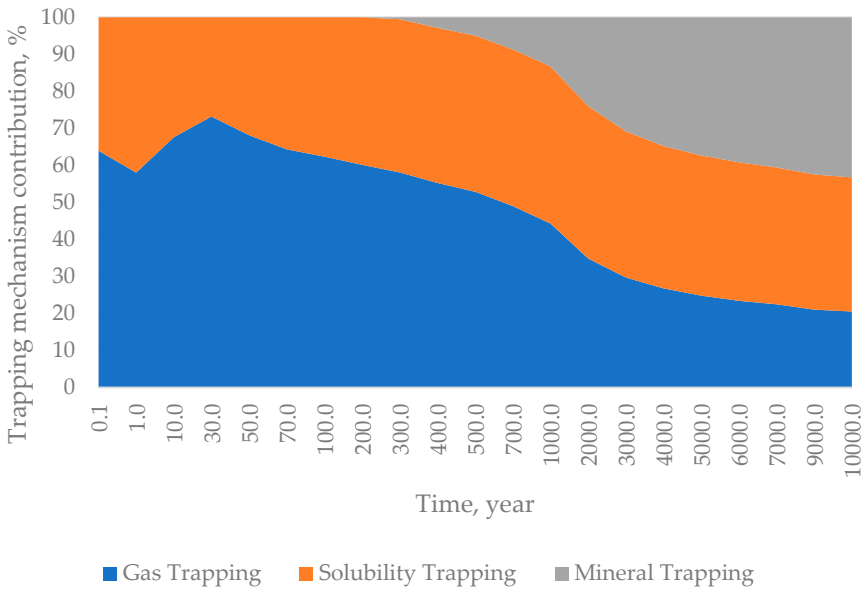


Figure 9. Graph showing contribution of different trapping mechanisms for base case through time.

For the homogeneous case, solubility trapping begins at ~45% and decreases to 35% at ~1 year. (Figure 10). After that, it decreases to ~30% at 10 years and increases gradually during post-injection until the end of the simulation, where it reaches 47%. Mineral trapping does not occur until ~500 years. Its percentage gradually increases to ~25% at 10,000 years. More than half of the injected CO_2 is in gas form until ~1000 years. After that, gas trapping gradually decreases to ~28% at the end of the simulation.

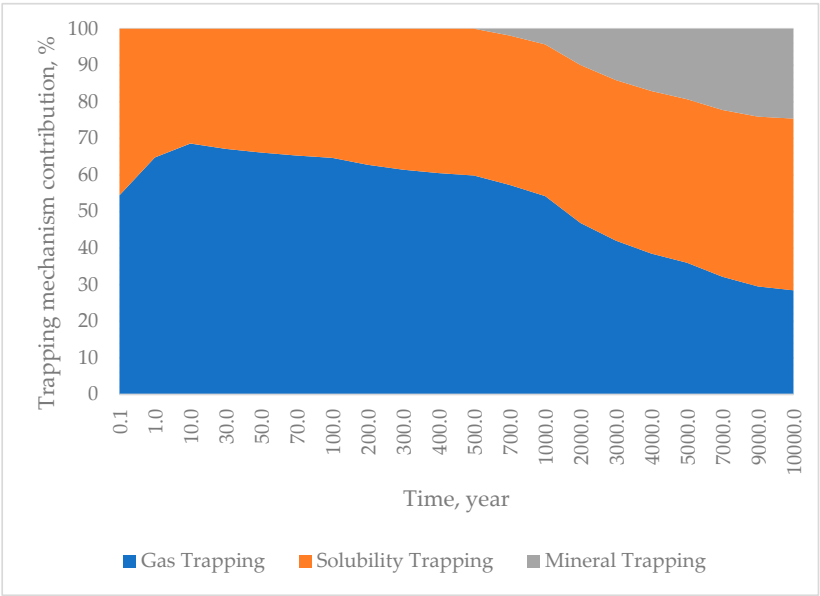


Figure 10. Graph showing contribution of different trapping mechanisms for homogenous case through time.

The dominant trapping mechanism in the base case is mineral trapping (43%), while it is solubility trapping (47%) in the homogeneous case at the end of the simulation. Because the fraction of mineral trapping in the base case is higher than that in the homogeneous case (25%), CO_2 storage is more secure in the base case at the time scale of 10,000 years.

5. Conclusions

In this study, 3D high-resolution simulation facilitated by parallel computation on a supercomputer was conducted to investigate the impact of hydrogeological heterogeneity on reactive transport simulation of GCS in the Mt. Simon Sandstone.

Results from this study indicate that the inclusion of hydrogeological heterogeneity of a formation has a significant influence on carbon storage in 3D reservoir simulations, in terms of CO_2 plume migration pattern, CO_2-water-mineral interaction, reservoir quality, and CO_2 plume containment. Because of these findings, it is necessary to include hydrogeological heterogeneity in reactive transport simulation of GCS. Even if the full 3D reservoir heterogeneity parameters are not available, assigning several layers of lithofacies with the variations in porosity and permeability in the vertical direction is highly recommended. The results show that:

- The shape of the CO_2 plume is greatly affected by the incorporation of reservoir heterogeneity in reactive transport modeling. In the case of this study, including porosity and permeability heterogeneity resulted in a mushroom-shaped CO_2 plume that was contained in the lower third of the reservoir, compared to a pillar-shaped CO_2 plume for the homogeneous case that reached the reservoir top.
- The difference in mineral trapping is primarily related to the distribution of the CO_2 plume. The wider plume and lower pCO_2 in the base case caused coupled K-feldspar dissolution and illite precipitation (Equation (5)) to be dominant, while, in the homogenous case, more concentrated plume and higher pCO_2 resulted in coupled albite dissolution and dawsonite precipitation (Equation (6)) domination.
- Without considering reservoir heterogeneity, the coupled albite dissolution-dawsonite (and quartz) precipitation reaction becomes more important than coupled K-feldspar dissolution-illite precipitation reaction in the study site, especially near the injection well. As a result, dawsonite is the dominant secondary carbonate mineral in the homogenous case.
- Since including hydrogeological heterogeneity in reservoir modeling leads to higher estimates for mineral trapping and slower upward CO_2 migration, modeling results may indicate safer and more secure CO_2 storage when reservoir heterogeneity is considered.

Author Contributions: Conceptualization, B.S., P.L. and C.Z.; methodology, B.S. and P.L.; software, B.S.; validation, B.S., P.L., R.K. and C.Z.; formal analysis, B.S. and P.L.; investigation, B.S., P.L.; resources, B.S. and R.K.; data curation, B.S.; writing—original draft preparation, B.S. and P.L.; writing—review and editing, R.K. and C.Z.; visualization, B.S. and R.K.; supervision, C.Z.; project administration, B.S. and C.Z.; funding acquisition, B.S. All authors have read and agreed to the published version of the manuscript.

Funding: This research was supported by the Indiana Geological and Water Survey and did not receive any additional funding for any of the work described.

Institutional Review Board Statement: Not applicable.

Informed Consent Statement: Not applicable.

Acknowledgments: The authors would like to thank Christopher Korose and Steve Whittaker from the Illinois State Geological Survey for their review and suggestions for this publication, specifically as it relates to the geological settings and carbon capture and storage initiatives occurring in the Illinois Basin.

Conflicts of Interest: The authors declare no conflict of interest.

Appendix A

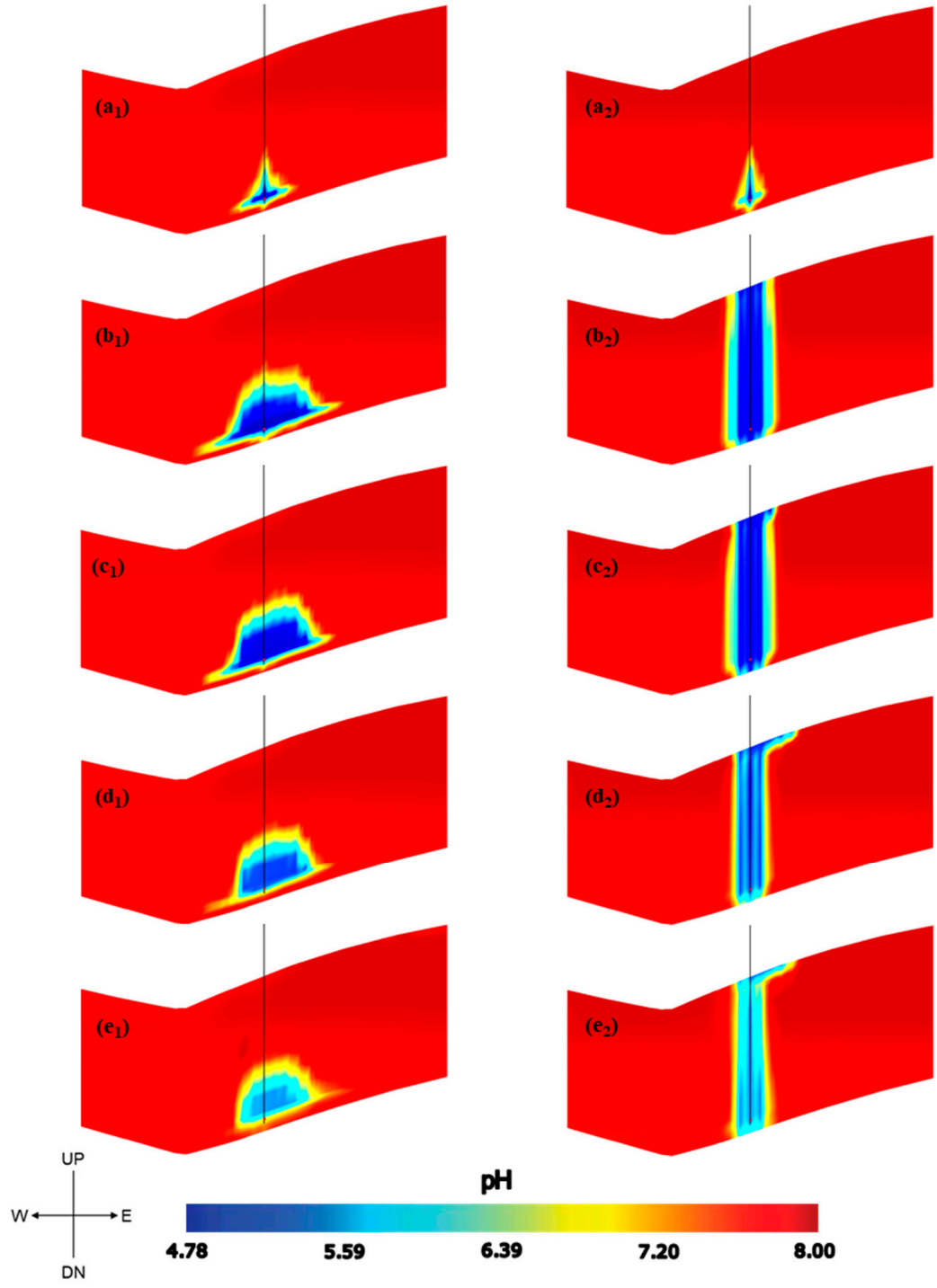


Figure A1. Fence diagrams illustrating the simulated pH evolution for the base case ($\mathbf{a_1}$,$\mathbf{b_1}$,$\mathbf{c_1}$,$\mathbf{d_1}$,$\mathbf{e_1}$) and homogeneous case ($\mathbf{a_2}$,$\mathbf{b_2}$,$\mathbf{c_2}$,$\mathbf{d_2}$,$\mathbf{e_2}$) at (**a**) 1 year, (**b**) 30 years, (**c**) 100 years, (**d**) 1000 years, and (**e**) 10,000 years. Each figure's size is approximately 35 km × 550 m (x, z).

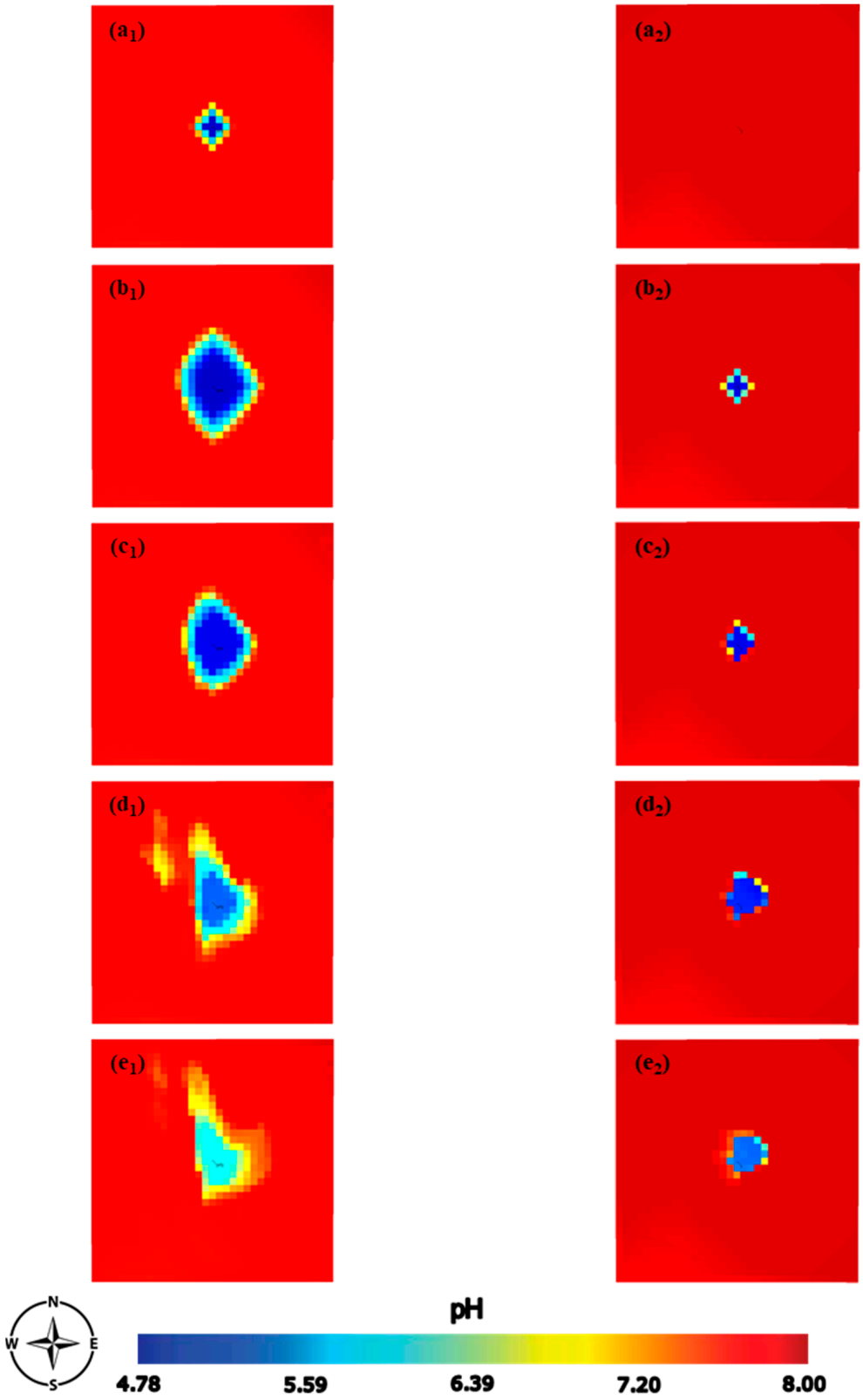


Figure A2. Plan view diagrams illustrating the simulated pH evolution for the base case from the arkosic layer top view ($\mathbf{a_1}$,$\mathbf{b_1}$,$\mathbf{c_1}$,$\mathbf{d_1}$,$\mathbf{e_1}$) and homogenous case from the Upper Mt. Simon top view ($\mathbf{a_2}$,$\mathbf{b_2}$,$\mathbf{c_2}$,$\mathbf{d_2}$,$\mathbf{e_2}$) at (**a**) 1 year, (**b**) 30 years, (**c**) 100 years, (**d**) 1000 years, and (**e**) 10,000 years. Each figure's size is 35 km × 35 km (x, y).

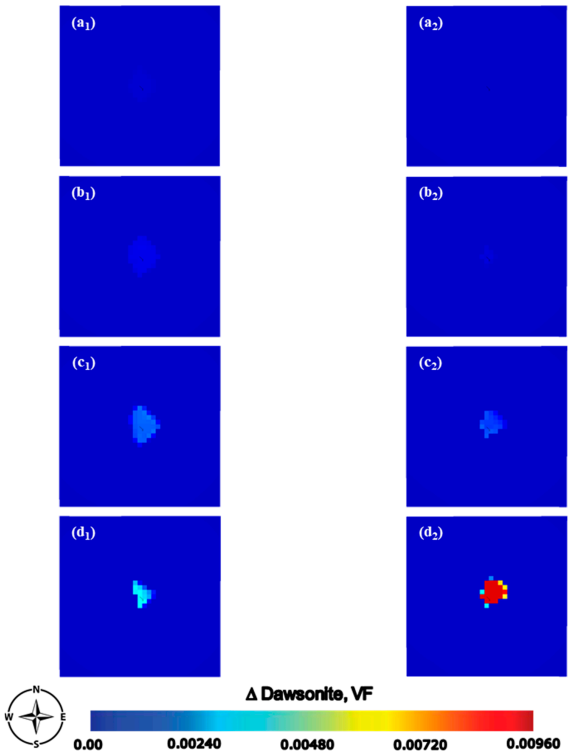


Figure A3. Plan view diagrams illustrating the simulated dawsonite volume fraction evolution for the base case from the arkosic layer top view ($\mathbf{a_1}$,$\mathbf{b_1}$,$\mathbf{c_1}$,$\mathbf{d_1}$) and homogenous case from the Upper Mt. Simon top view ($\mathbf{a_2}$,$\mathbf{b_2}$,$\mathbf{c_2}$,$\mathbf{d_2}$) at (**a**) 30 years, (**b**) 100 years, (**c**) 1000 years, and (**d**) 10,000 years. Each figure's size is 35 km × 35 km (x, y).

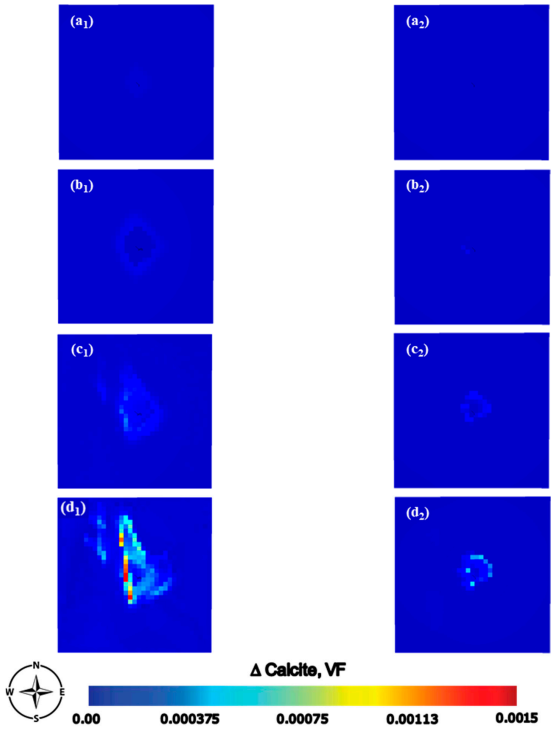


Figure A4. Plan view diagrams illustrating the simulated calcite volume fraction evolution for the base case from the arkosic layer top view ($\mathbf{a_1}$,$\mathbf{b_1}$,$\mathbf{c_1}$,$\mathbf{d_1}$) and homogenous case from the Upper Mt. Simon top view ($\mathbf{a_2}$,$\mathbf{b_2}$,$\mathbf{c_2}$,$\mathbf{d_2}$) at (**a**) 30 years, (**b**) 100 years, (**c**) 1000 years, and (**d**) 10,000 years. Each figure's size is 35 km × 35 km (x, y).

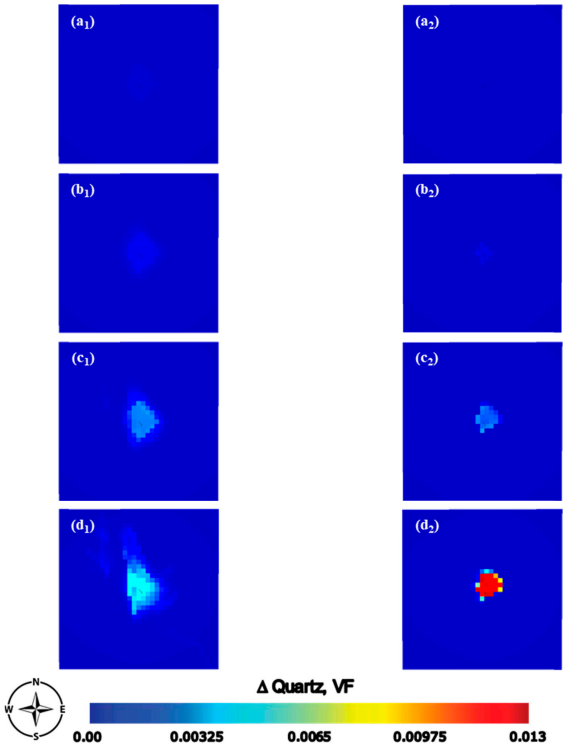


Figure A5. Plan view diagrams illustrating the simulated Δ quartz volume fraction evolution for the base case from the arkosic layer top view ($\mathbf{a_1}$,$\mathbf{b_1}$,$\mathbf{c_1}$,$\mathbf{d_1}$) and homogenous case from the Upper Mt. Simon top view ($\mathbf{a_2}$,$\mathbf{b_2}$,$\mathbf{c_2}$,$\mathbf{d_2}$) at (**a**) 30 years, (**b**) 100 years, (**c**) 1000 years, and (**d**) 10,000 years. Each figure's size is 35 km × 35 km (x, y).

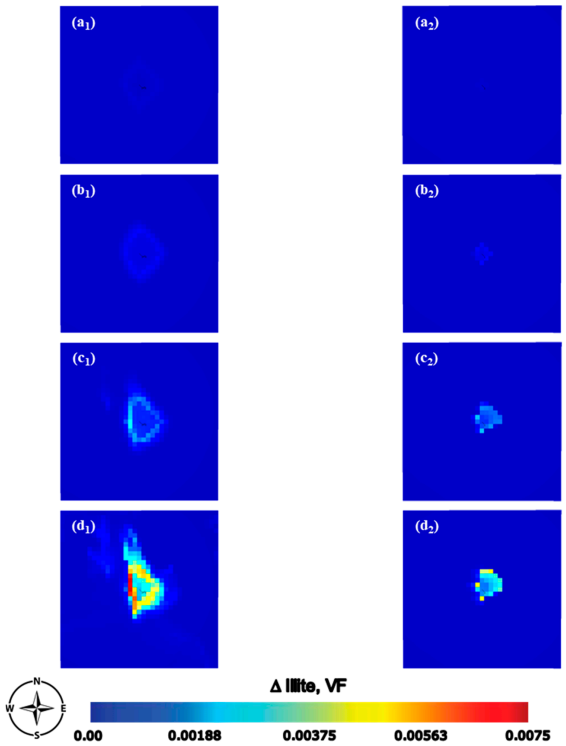


Figure A6. Plan view diagrams illustrating the simulated Δ illite volume fraction evolution for the base case from the arkosic layer top view ($\mathbf{a_1}$,$\mathbf{b_1}$,$\mathbf{c_1}$,$\mathbf{d_1}$) and homogenous case from the Upper Mt. Simon top view ($\mathbf{a_2}$,$\mathbf{b_2}$,$\mathbf{c_2}$,$\mathbf{d_2}$) at (**a**) 30 years, (**b**) 100 years, (**c**) 1000 years, and (**d**) 10,000 years. Each figure's size is 35 km × 35 km (x, y).

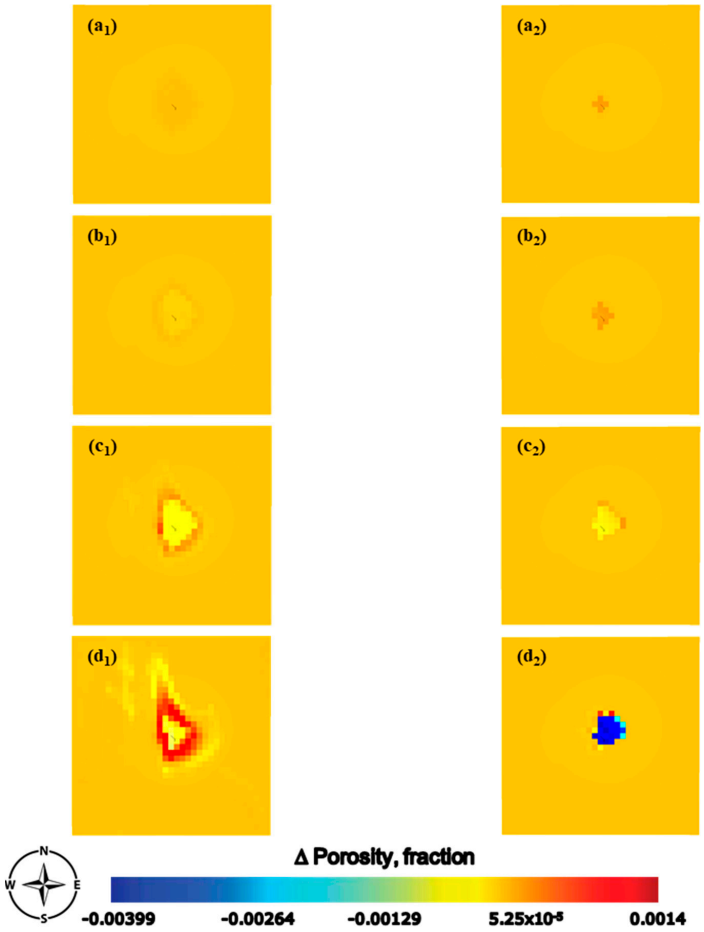


Figure A7. Plan view diagrams illustrating the simulated Δ porosity evolution for the base case from the arkosic layer top view ($\mathbf{a_1}$,$\mathbf{b_1}$,$\mathbf{c_1}$,$\mathbf{d_1}$) and homogenous case from the Upper Mt. Simon top view ($\mathbf{a_2}$,$\mathbf{b_2}$,$\mathbf{c_2}$,$\mathbf{d_2}$) at (**a**) 30 years, (**b**) 100 years, (**c**) 1000 years, and (**d**) 10,000 years. Each figure's size is 35 km × 35 km (x, y).

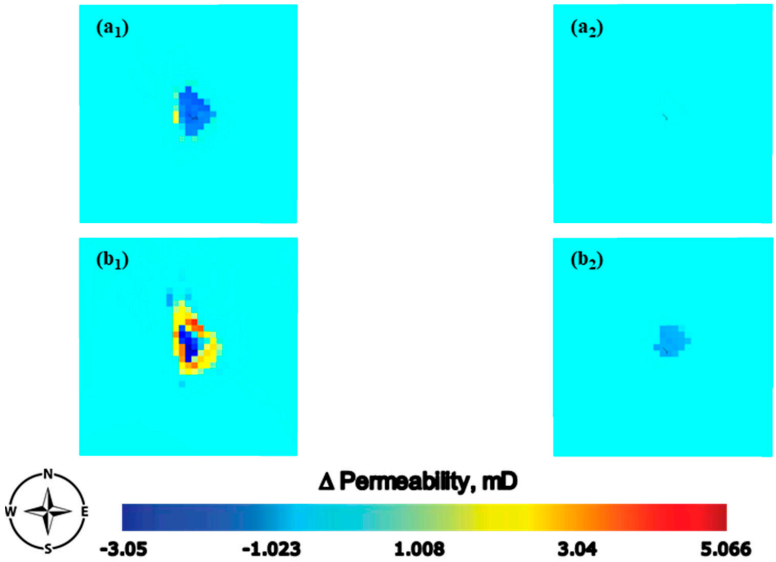


Figure A8. Plan view diagrams illustrating the simulated Δ permeability evolution for the base case from the arkosic layer top view ($\mathbf{a_1}$,$\mathbf{b_1}$) and homogenous case from the Upper Mt. Simon top view ($\mathbf{a_2}$,$\mathbf{b_2}$) at (**a**) 1000 years, and (**b**) 10,000 years. Each figure's size is 35 km × 35 km (x, y).

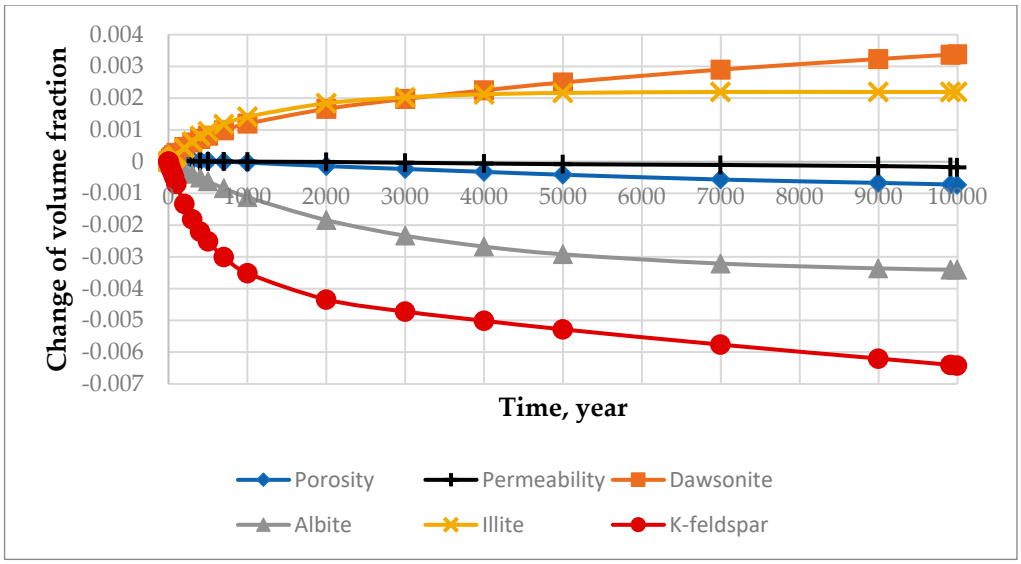


Figure A9. Change in volume fraction of different minerals in the base case along with porosity and permeability alteration near the injection well in the arkosic layer throughout the 10,000 years of simulation. Change in permeability is in Darcy.

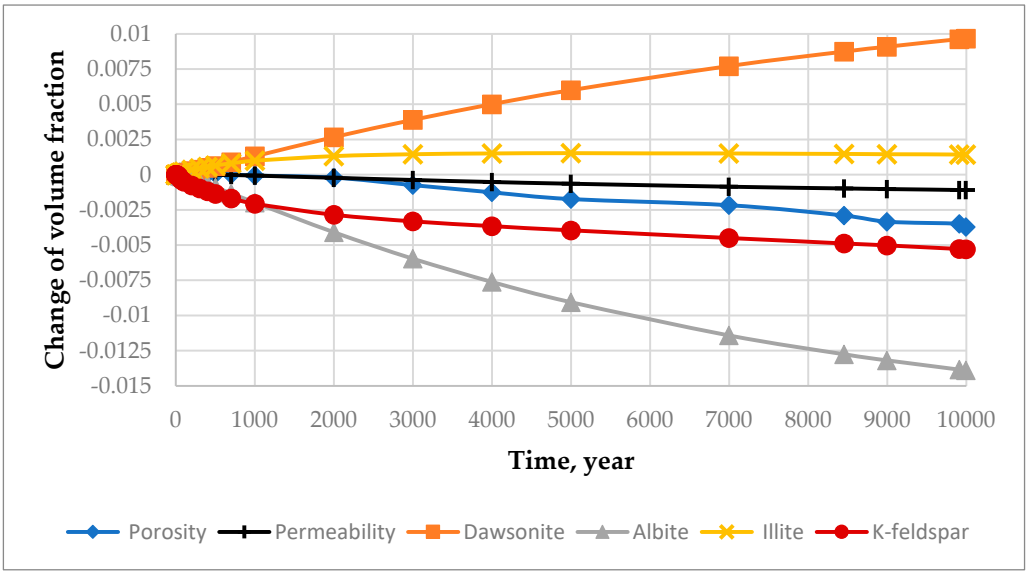


Figure A10. Change in volume fraction of different minerals in the homogenous case along with porosity and permeability alteration near the injection well in reservoir's uppermost layer throughout the 10,000 years of simulation. Change in permeability is in Darcy.

References

1. Shabani, B.; Vilcáez, J. Prediction of CO_2-CH_4-H_2S-N_2 gas mixtures solubility in brine using a non-iterative fugacity-activity model relevant to CO_2-MEOR. *J. Pet. Sci. Eng.* **2017**, *150*, 162–179. [CrossRef]
2. Bachu, S. CO_2 storage in geological media: Role, means, status and barriers to deployment. *Prog. Energy Combust. Sci.* **2008**, *34*, 254–273. [CrossRef]
3. IPCC. IPCC Special Report on Carbon Dioxide Capture and Storage. In *Prepared by Working Group III of the Intergovernmental Panel on Climate Change*; Bert Metz, O.D., de Coninck, H., Loos, M., Meyer, L., Eds.; Cambridge University Press: Cambridge, UK, 2005.
4. Atlas, C.S. Carbon Storage Atlas; U.S. Department of Energy, Office of Fossil Energy. 2015. Available online: https://www.netl.doe.gov/sites/default/files/2018-10/ATLAS-V-2015.pdf (accessed on 7 March 2022).
5. Xu, T.; Sonnenthal, E.; Spycher, N.; Pruess, K. Toughreact—A simulation program for non-isothermal multiphase reactive geochemical transport in variably saturated geologic media: Applications to geothermal injectivity and CO_2 geological sequestration. *Comput. Geosci.* **2006**, *32*, 145–165. [CrossRef]

6. Steefel, C.; Appelo, C.; Arora, B.; Jacques, D.; Kalbacher, T.; Kolditz, O.; Lagneau, V.; Lichtner, P.; Mayer, K.U.; Meeussen, J. Reactive transport codes for subsurface environmental simulation. *Comput. Geosci.* **2015**, *19*, 445–478. [CrossRef]
7. Shabani, B.; Vilcáez, J. Toughreact-Co_2bio–A new module to simulate geological carbon storage under biotic conditions (Part 1): The multiphase flow of CO_2-CH_4-H_2-H_2S gas mixtures. *J. Nat. Gas Sci. Eng.* **2019**, *63*, 85–94. [CrossRef]
8. Smith, M.; Hao, Y.; Carroll, S. Development and calibration of a reactive transport model for carbonate reservoir porosity and permeability changes based on CO_2 core-flood experiments. *Int. J. Greenh. Gas Control* **2017**, *57*, 73–88. [CrossRef]
9. Johnson, J.W.; Nitao, J.J.; Knauss, K.G. Reactive transport modelling of CO_2 storage in saline aquifers to elucidate fundamental processes, trapping mechanisms and sequestration partitioning. *Geol. Soc. Lond. Spec. Publ.* **2004**, *233*, 107–128. [CrossRef]
10. Liu, F.; Lu, P.; Zhu, C.; Xiao, Y. Coupled reactive flow and transport modeling of CO_2 sequestration in the Mt. Simon sandstone formation, Midwest USA. *Int. J. Greenh. Gas Control* **2011**, *5*, 294–307. [CrossRef]
11. Zhu, C.; Zhang, G.; Lu, P.; Meng, L.; Ji, X. Benchmark modeling of the Sleipner CO_2 plume: Calibration to seismic data for the uppermost layer and model sensitivity analysis. *Int. J. Greenh. Gas Control* **2015**, *43*, 233–246. [CrossRef]
12. Shabani, B.; Pashin, J.; Vilcáez, J. TOUGHREACT-CO2Bio–A new module to simulate geological carbon storage under biotic conditions (Part 2): The bio-geochemical reactive transport of CO_2-CH_4-H_2-H_2S gas mixtures. *J. Nat. Gas Sci. Eng.* **2020**, *76*, 103190. [CrossRef]
13. Zhang, G.; Lu, P.; Wei, X.; Zhu, C. Impacts of mineral reaction kinetics and regional groundwater flow on long-term CO_2 fate at Sleipner. *Energy Fuels* **2016**, *30*, 4159–4180. [CrossRef]
14. Zhang, G.; Lu, P.; Zhang, Y.; Wei, X.; Zhu, C. Effects of rate law formulation on predicting CO_2 sequestration in sandstone formations. *Int. J. Energy Res.* **2015**, *39*, 1890–1908. [CrossRef]
15. Tian, L.; Yang, Z.; Fagerlund, F.; Niemi, A. Effects of permeability heterogeneity on CO_2 injectivity and storage efficiency coefficient. *Greenh. Gases Sci. Technol.* **2016**, *6*, 112–124. [CrossRef]
16. Deng, H.; Stauffer, P.H.; Dai, Z.; Jiao, Z.; Surdam, R.C. Simulation of industrial-scale CO_2 storage: Multi-scale heterogeneity and its impacts on storage capacity, injectivity and leakage. *Int. J. Greenh. Gas Control* **2012**, *10*, 397–418. [CrossRef]
17. Goater, A.L.; Bijeljic, B.; Blunt, M.J. Dipping open aquifers—The effect of top-surface topography and heterogeneity on CO_2 storage efficiency. *Int. J. Greenh. Gas Control* **2013**, *17*, 318–331. [CrossRef]
18. Tian, H.; Pan, F.; Xu, T.; McPherson, B.J.; Yue, G.; Mandalaparty, P. Impacts of hydrological heterogeneities on caprock mineral alteration and containment of CO_2 in geological storage sites. *Int. J. Greenh. Gas Control* **2014**, *24*, 30–42. [CrossRef]
19. Flett, M.; Gurton, R.; Weir, G. Heterogeneous saline formations for carbon dioxide disposal: Impact of varying heterogeneity on containment and trapping. *J. Pet. Sci. Eng.* **2007**, *57*, 106–118. [CrossRef]
20. Zhao, R.; Cheng, J.; Zhang, K. CO_2 plume evolution and pressure buildup of large-scale CO_2 injection into saline aquifers in Sanzhao Depression, Songliao Basin, China. *Transp. Porous Media* **2012**, *95*, 407–424. [CrossRef]
21. Lengler, U.; De Lucia, M.; Kühn, M. The impact of heterogeneity on the distribution of CO_2: Numerical simulation of CO_2 storage at Ketzin. *Int. J. Greenh. Gas Control* **2010**, *4*, 1016–1025. [CrossRef]
22. Sarkarfarshi, M.; Malekzadeh, F.A.; Gracie, R.; Dusseault, M.B. Parametric sensitivity analysis for CO_2 geosequestration. *Int. J. Greenh. Gas Control* **2014**, *23*, 61–71. [CrossRef]
23. Williams, G.; Chadwick, R. Influence of reservoir-scale heterogeneities on the growth, evolution and migration of a CO_2 plume at the Sleipner Field, Norwegian North Sea. *Int. J. Greenh. Gas Control* **2021**, *106*, 103260. [CrossRef]
24. Hovorka, S.D.; Doughty, C.; Benson, S.M.; Pruess, K.; Knox, P.R. The impact of geological heterogeneity on CO_2 storage in brine formations: A case study from the Texas Gulf Coast. *Geol. Soc. Lond. Spec. Publ.* **2004**, *233*, 147–163. [CrossRef]
25. Hitchon, B. *Aquifer Disposal of Carbon Dioxide: Hydrodynamic and Mineral Trapping-Proof of Concept*; Geoscience Publishing Ltd.: Sherwood Park, AB, Canada, 1996.
26. Zhang, D.; Song, J. Mechanisms for geological carbon sequestration. *Procedia IUTAM* **2014**, *10*, 319–327. [CrossRef]
27. Shabani, B.; Vilcáez, J. A fast and robust TOUGH2 module to simulate geological CO_2 storage in saline aquifers. *Comput. Geosci.* **2018**, *111*, 58–66. [CrossRef]
28. Hermanson, J.L. Multiphase Flow and Reactive Transport Modelling of CO_2 Storage in Heterogeneous Reservoirs. Science: Department of Earth Sciences. 2013. Available online: http://summit.sfu.ca/item/13895 (accessed on 7 March 2022).
29. Dai, Z.; Xu, L.; Xiao, T.; McPherson, B.; Zhang, X.; Zheng, L.; Dong, S.; Yang, Z.; Soltanian, M.R.; Yang, C. Reactive chemical transport simulations of geologic carbon sequestration: Methods and applications. *Earth-Sci. Rev.* **2020**, *208*, 103265. [CrossRef]
30. Becker, L.E.; Le, B.; Ta, D. *Pre-Knox (Cambrian) Stratigraphy in Indiana*; Indiana Geological Survey: Bloomington, IN, USA, 1978.
31. Medina, C.R.; Rupp, J.A. Reservoir characterization and lithostratigraphic division of the Mount Simon Sandstone (Cambrian): Implications for estimations of geologic sequestration storage capacity. *Environ. Geosci.* **2012**, *19*, 1–15. [CrossRef]
32. Leetaru, H.E.; McBride, J.H. Reservoir uncertainty, Precambrian topography, and carbon sequestration in the Mt. Simon Sandstone, Illinois Basin. *Environ. Geosci.* **2009**, *16*, 235–243. [CrossRef]
33. Bowen, B.B.; Ochoa, R.I.; Wilkens, N.D.; Brophy, J.; Lovell, T.R.; Fischietto, N.; Medina, C.R.; Rupp, J.A. Depositional and diagenetic variability within the Cambrian Mount Simon Sandstone: Implications for carbon dioxide sequestration. *Environ. Geosci.* **2011**, *18*, 69–89. [CrossRef]
34. Natcarb/Atlas. Natcarb/Atlas; U.S. Department of Energy–National Energy Technology Laboratory. 2015. Available online: https://www.netl.doe.gov/coal/carbon-storage/strategic-program-support/natcarb-atlas (accessed on 7 March 2022).

35. Lahann, R.; Rupp, J.; Medina, C. An evaluation of the seal capacity and CO_2 retention properties of the Eau Claire Formation (Cambrian). *Environ. Geosci.* **2014**, *21*, 83–106. [CrossRef]
36. Leetaru, H.E.; Brown, A.; Lee, D.; Senel, O.; Couëslan, M. CO_2 Injectivity, Storage Capacity, Plume Size, and Reservoir and Seal Integrity of the Ordovician St. Peter Sandstone and the Cambrian Potosi Formation in the Illinos Basin. 2012. Available online: https://experts.illinois.edu/en/publications/co2-injectivity-storage-capacity-plume-size-and-reservoir-and-sea (accessed on 7 March 2022).
37. Will, R.; Smith, V.; Leetaru, H. *Utilization of the St. Peter Sandstone in the Illinois Basin for CO_2 Sequestration*; University of Illinois: Urbana-Champaign, IL, USA, 2014.
38. Barnes, D.A.; Ellett, K.M.; Rupp, J.A. Geologic-carbon-sequestration potential of the Ordovician St. Peter Sandstone, Michigan and Illinois Basins, United States. *Environ. Geosci.* **2017**, *24*, 15–49. [CrossRef]
39. Harris, D.; Ellett, K.; Rupp, J.; Leetaru, H. *Geologic Characterization and Carbon Storage Resource Estimates for the Knox Group, Illinois Basin, Illinois, Indiana and Kentucky*; University of Illinois: Urbana-Champaign, IL, USA, 2014.
40. Dapples, E.C. General lithofacies relationship of St. Peter Sandstone and Simpson Group. *AAPG Bull.* **1955**, *39*, 444–467.
41. Pitman, J.K.; Goldhaber, M.B.; Spöetl, C. Regional Diagenetic Patterns in the St. Peter Sandstone: Implications for Brine Migration in the Illinois Basin; US Government Printing Office. 1997. Available online: https://pubs.usgs.gov/bul/b2094a/b2094a.pdf (accessed on 7 March 2022).
42. Greb, S.F.; Bowersox, J.R.; Solis, M.P.; Harris, D.C.; Riley, R.A.; Rupp, J.A.; Kelley, M.; Gupta, N. Ordovician Knox Carbonates and Sandstones of the Eastern Mid-Continent: Potential Geologic Carbon Storage Reservoirs and Seals. 2012. Available online: https://archives.datapages.com/data/specpubs/memoir98/CHAPTER45/CHAPTER45.HTM (accessed on 7 March 2022).
43. Medina, C.R.; Mastalerz, M.; Lahann, R.W.; Rupp, J.A. A novel multi-technique approach used in the petrophysical characterization of the Maquoketa Group (Ordovician) in the southeastern portion of the Illinois Basin: Implications for seal efficiency for the geologic sequestration of CO_2. *Int. J. Greenh. Gas Control* **2020**, *93*, 102883. [CrossRef]
44. Greenberg, S.E.; Bauer, R.; Will, R.; Locke II, R.; Carney, M.; Leetaru, H.; Medler, J. Geologic carbon storage at a one million tonne demonstration project: Lessons learned from the Illinois Basin–Decatur Project. *Energy Procedia* **2017**, *114*, 5529–5539. [CrossRef]
45. Freiburg, J.T.; Leetaru, H.E.; Monson, C.C. The Argenta Formation; a newly recognized Cambrian stratigraphic unit in the Illinois Basin. In Proceedings of the Abstracts with Programs–Geological Society of America, Baltimore, MD, USA, 1–4 November 2015; p. 86.
46. Freiburg, J.T.; Ritzi, R.W.; Kehoe, K.S. Depositional and diagenetic controls on anomalously high porosity within a deeply buried CO_2 storage reservoir—The Cambrian Mt. Simon Sandstone, Illinois Basin, USA. *Int. J. Greenh. Gas Control* **2016**, *55*, 42–54. [CrossRef]
47. Carbonsafe, W. Wabash Carbonsafe. Available online: https://www.netl.doe.gov/projects/project-information.aspx?p=FE0031626 (accessed on 7 March 2022).
48. Resources, W.V. Wabash Valley Resources. Available online: https://www.wvresc.com/ (accessed on 7 March 2022).
49. Blakley, C.; Carman, C.; Leetaru, H.; Korose, C. *CarbonSAFE East Sub-Basin Site Feasibility Plan Subtask 4.5–Topical Report: DOE-FE0029445-12*; University of Illinois: Urbana-Champaign, IL, USA, 2019.
50. Gupta, N.; Ball, D.; Jagucki, P.; Bradbury, J. Validating Geologic Storage Potential in the Midwestern USA through Multiple Field Demonstrations. *Energy Procedia* **2009**, *1*, 2063–2069. [CrossRef]
51. Medina, C.R.; Rupp, J.A.; Barnes, D.A. Effects of reduction in porosity and permeability with depth on storage capacity and injectivity in deep saline aquifers: A case study from the Mount Simon Sandstone aquifer. *Int. J. Greenh. Gas Control.* **2011**, *5*, 146–156. [CrossRef]
52. Ellett, K.; Zhang, Q.; Medina, C.; Rupp, J.; Wang, G.; Carr, T. Uncertainty in regional-scale evaluation of CO_2 geologic storage resources—Comparison of the Illinois Basin (USA) and the Ordos Basin (China). *Energy Procedia* **2013**, *37*, 5151–5159. [CrossRef]
53. Xu, T.; Sonnenthal, E.; Spycher, N.; Zheng, L. *Toughreact V3.0-OMP Reference Manual: A Parallel Simulation Program for Non-Isothermal Multiphase Geochemical Reactive Transport*; University of California: Berkeley, CA, USA, 2014.
54. Pruess, K.; Spycher, N. ECO2N–A fluid property module for the TOUGH2 code for studies of CO_2 storage in saline aquifers. *Energy Convers. Manag.* **2007**, *48*, 1761–1767. [CrossRef]
55. Frailey, S.M.; Damico, J.; Leetaru, H.E. Reservoir characterization of the Mt. Simon Sandstone, Illinois Basin, USA. *Energy Procedia* **2011**, *4*, 5487–5494. [CrossRef]
56. Xu, T.; Apps, J.A.; Pruess, K.; Yamamoto, H. Numerical modeling of injection and mineral trapping of CO_2 with H_2S and SO_2 in a sandstone formation. *Chem. Geol.* **2007**, *242*, 319–346. [CrossRef]
57. Labotka, D.M.; Panno, S.V.; Locke, R.A.; Freiburg, J.T. Isotopic and geochemical characterization of fossil brines of the Cambrian Mt. Simon Sandstone and Ironton–Galesville Formation from the Illinois Basin, USA. *Geochim. Cosmochim. Acta* **2015**, *165*, 342–360. [CrossRef]
58. Salih, H.H.; Dastgheib, S.A. Treatment of a hypersaline brine, extracted from a potential CO_2 sequestration site, and an industrial wastewater by membrane distillation and forward osmosis. *Chem. Eng. J.* **2017**, *325*, 415–423. [CrossRef]
59. Palandri, J.L.; Kharaka, Y.K. A Compilation of Rate Parameters of Water-Mineral Interaction Kinetics for Application to Geochemical Modeling. *U.S. Geol. Surv.* **2004**, *66*. [CrossRef]
60. Marty, N.C.; Claret, F.; Lassin, A.; Tremosa, J.; Blanc, P.; Madé, B.; Giffaut, E.; Cochepin, B.; Tournassat, C. A database of dissolution and precipitation rates for clay-rocks minerals. *Appl. Geochem.* **2015**, *55*, 108–118. [CrossRef]

61. Smith, M.M.; Carroll, S.A. Chlorite dissolution kinetics at pH 3–10 and temperature to 275 °C. *Chem. Geol.* **2016**, *421*, 55–64. [CrossRef]
62. Rimstidt, J.D. *Geochemical Rate Models: An Introduction to Geochemical Kinetics*; Cambridge University Press: Cambridge, UK, 2014. Available online: https://www.cambridge.org/core/books/geochemical-rate-models/A870104C3EA1B238E00EA96ED0A26B3D (accessed on 7 March 2022).
63. Zhu, C.; Anderson, G.; Burden, D.S. *Environmental Applications of Geochemical Modeling*; Cambridge University Press: Cambridge, UK, 2002.
64. Lasaga, A.C. *Kinetic Theory in the Earth Sciences*; Princeton University Press: Princeton, NJ, USA, 2014.
65. Hellevang, H.; Aagaard, P.; Oelkers, E.H.; Kvamme, B. Can dawsonite permanently trap CO_2? *Environ. Sci. Technol.* **2005**, *39*, 8281–8287. [CrossRef]
66. Metz, B.; Davidson, O.; De Coninck, H. *Carbon Dioxide Capture and Storage: Special Report of the Intergovernmental Panel on Climate Change*; Cambridge University Press: Cambridge, UK, 2005. Available online: https://www.ipcc.ch/site/assets/uploads/2018/03/srccs_wholereport-1.pdf (accessed on 7 March 2022).